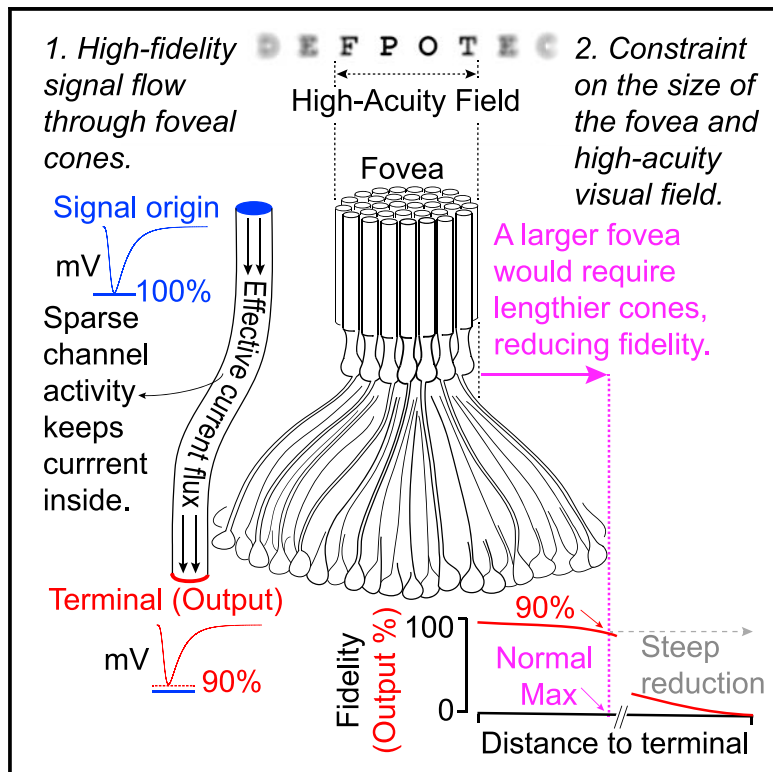


Optimized Signal Flow through Photoreceptors Supports the High-Acuity Vision of Primates

Graphical Abstract



Authors

Gregory S. Bryman, Andreas Liu,
Michael Tri H. Do

Correspondence

gsbryman@gmail.com (G.S.B.),
michael.do@childrens.harvard.edu (M.T.H.D.)

In Brief

Humans and other primates outstrip most animals in their sharpness of vision. This performance originates with the fine-grained array of photoreceptors in the primate fovea. Bryman et al. investigate form and function relationships within these neurons, revealing biophysical optimizations for high-fidelity signaling and constraints on the evolution of foveal size.

Highlights

- Despite their shape, primate foveal photoreceptors propagate signals with fidelity
- High-fidelity signal propagation is independent of amplification
- Optimizations of intracellular and membrane conductivities support propagation
- Biophysical limits help explain the conservation of foveal size across species

Article

Optimized Signal Flow through Photoreceptors Supports the High-Acuity Vision of Primates

Gregory S. Bryman,^{1,*} Andreas Liu,¹ and Michael Tri H. Do^{1,2,*}

¹F.M. Kirby Neurobiology Center and Department of Neurology, Boston Children's Hospital and Harvard Medical School, Center for Life Science 12061, 3 Blackfan Circle, Boston, MA 02115, USA

²Lead Contact

*Correspondence: gbsbryman@gmail.com (G.S.B.), michael.do@childrens.harvard.edu (M.T.H.D.)

<https://doi.org/10.1016/j.neuron.2020.07.035>

SUMMARY

The fovea is a neural specialization that endows humans and other primates with the sharpest vision among mammals. This performance originates in the foveal cones, which are extremely narrow and long to form a high-resolution pixel array. Puzzlingly, this form is predicted to impede electrical conduction to an extent that appears incompatible with vision. We observe the opposite: signal flow through even the longest cones (0.4-mm axons) is essentially lossless. Unlike in most neurons, amplification and impulse generation by voltage-gated channels are dispensable. Rather, sparse channel activity preserves intracellular current, which flows as if unobstructed by organelles. Despite these optimizations, signaling would degrade if cones were lengthier. Because cellular packing requires that cone elongation accompanies foveal expansion, this degradation helps explain why the fovea is a constant, minuscule size despite multiplicative changes in eye size through evolution. These observations reveal how biophysical mechanisms tailor form-function relationships for primate behavioral performance.

INTRODUCTION

Humans and other primates see a combination of spatial detail and contrast that has few peers in the animal kingdom (Caves et al., 2018; Harmening, 2017; Veilleux and Kirk, 2014). This performance originates in the fovea, a feature of the retina that is lacked by other mammals. The fovea composes <1% of the retinal surface area. Nevertheless, it is required for daily tasks like reading and recognizing faces. Its signals occupy a third of the optic nerve and half of primary visual cortex to generate much of conscious vision (Polyak, 1941; Rodieck, 1998; Van Essen et al., 1984). The importance of the fovea is also underscored by the devastating effects of macular degeneration, a leading cause of blindness—the fovea is the center of the macula (Ambati and Fowler, 2012; Vugler, 2010). With only the peripheral retina available for vision, one is legally blind (Masland, 2017).

A crucial specialization of the fovea is its distinct complement of cone photoreceptors, the neurons that transduce light into electrical signals (Dowling, 1965; Peng et al., 2019; Polyak, 1941; Sinha et al., 2017). These cones are slender and tightly packed to form a uniquely fine detector array (Figures 1A and 1B; Polyak, 1941). Downstream neurons are larger, more numerous, and displaced laterally (Schein, 1988). Foveal cones therefore extend axons for hundreds of microns to make contact (Figure 1A; Drasdo et al., 2007; Perry and Cowey, 1988). Electrical signals are generated at the outer segment (OS) and must propagate through the elongated inner segment (IS) and axon

to drive activity in circuits of the retina and brain. Thus, the nature of propagation determines the information that underlies the exceptional vision of primates. Long-distance propagation is generally understood to rely on the production of regenerative spikes, but vertebrate photoreceptors are thought to signal almost exclusively with graded changes in voltage rather than spikes (Van Hook et al., 2019). How foveal cones propagate signals is unknown, reflecting a general lack of knowledge concerning the relationships of cellular form and function in the primate nervous system (Beaulieu-Laroche et al., 2018; Eyal et al., 2016; Gidon et al., 2020).

The most direct examination of signal propagation through foveal cones is a computational simulation that used realistic anatomy but omitted voltage-gated ion channels and adopted biophysical parameters from other neurons. The conclusion was that the signal becomes minuscule as it propagates (Hsu et al., 1998). This view is reinforced by the only previous study of current flow through vertebrate photoreceptors, which found that the intracellular conductivity of turtle cones was extremely low (Lasater et al., 1989). Existing biophysical information therefore suggests that signals are severely attenuated and slowed by propagation through foveal cones (Figures 1C–1E). This degree of attenuation appears incompatible with the voltage dependence of synaptic release and the high contrast sensitivity of primate vision (Figure 1D). Severe slowing is also unexpected: downstream of foveal cones, the responses of retinal output neurons rise with little delay and, overall, match the kinetics of

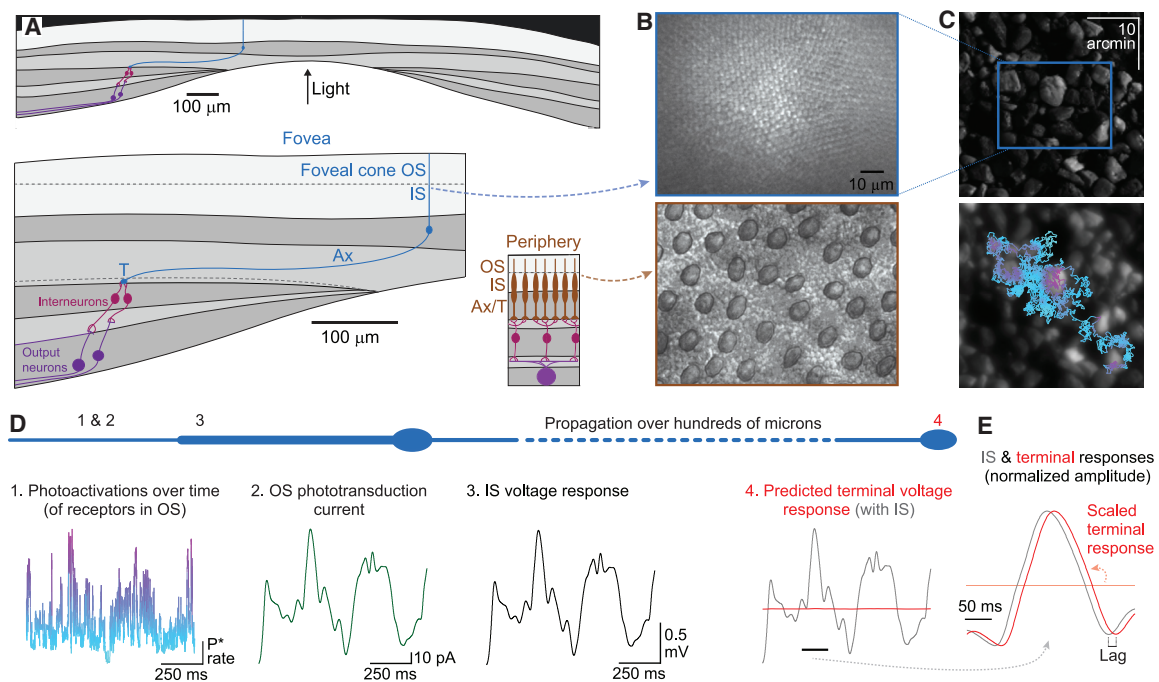


Figure 1. Form and Function in Primate Foveal Cones: The Expectation of Low-Fidelity Signal Propagation

(A) Schematic of the primate retina in cross section, centered on the fovea (top). The foveal pit gives cones direct access to light. Magnification is shown below, with peripheral retina schematic. The outer segment (OS) transduces light into an electrical response, which propagates through the inner segment (IS), soma, and axon (Ax) to reach the terminal (T) for synaptic transmission. In the fovea, each cone has dedicated downstream neurons. In the periphery, multiple cones converge onto downstream neurons (rods are not shown).

(B) Photoreceptors viewed en face in the live macaque retina at the central fovea (top; all are cones) and periphery (bottom; larger cells are cones, interspersed with rods). Lines from (A) indicate focal planes.

(C) (Top) A calibrated photograph of a natural scene (pebbled ground) that contains high spatial detail (van Hateren and van der Schaaf, 1998). (Bottom) The scene is filtered by a representation of the eye's optics at the fovea and jittered over the receptive field of a simulated foveal cone by modeled eye movements (overlay shows receptive field position every 0.1 ms over 2 s; STAR Methods). The result is a dynamic rate of photoactivated receptor molecules at the OS, from low (blue) to high (violet), as shown by the vertical scale on the left in (D).

(D) In a simulated foveal cone, photoactivations (P^*) in the OS (1) are transduced into an electrical current (2), resulting in a modulation of voltage at the adjoining IS (3). The response at the distant presynaptic terminal (4) is predicted to be severely attenuated by propagation. This simulation uses a passive compartmental model of a foveal cone that possesses realistic morphology. Membrane conductivity is estimated from macaque peripheral cones (Schneeweis and Schnapf, 1999) and internal conductivity from turtle cones (the only existing estimate of this parameter in photoreceptors; Lasater et al., 1989). The length of the scale bar for P^* rate is 50,000 P^*/s , and the color scale is matched to (C).

(E) Scaling the simulated terminal response to highlight its expected time lag, which is too long to be compatible with measured response latencies in visual circuitry (Sinha et al., 2017). A previous model of propagation through foveal cones also predicts strong attenuation (e.g., ~10-fold at 60 Hz; Hsu et al., 1998).

phototransduction (Sinha et al., 2017; Figure 1E). The goal of the present study is to directly observe signal propagation through foveal cones, determine the underlying mechanisms, and address the implications for vision.

RESULTS

High-Fidelity Signal Propagation through Foveal Cones

To directly examine signal propagation through foveal cones, we isolated these cells from the macaque retina and made simultaneous electrophysiological recordings from the IS and presynaptic terminal (Figures 2A and S1). Foveal cones of different lengths were recovered, as expected from their known morphological variety (Perry and Cowey, 1988). We compared these cells to peripheral cones, which are short and stout (Figure 2A, right). The absence of an OS was typical in dissociated cones but unlikely

to affect our findings (see below and Figure S6). Otherwise, dissociation caused no detectable aberrations in biophysical properties, with membrane responses appearing normal whether they were passive (compare Figure 4G with S5B and see Figures 5C–E) or active (Figure S2) in origin. Also innocuous was perturbation of cytosol by the “whole-cell” mode of electrophysiological recording used here (Figure 7; STAR Methods).

We injected electrical current into the IS and compared the voltage responses at the IS and terminal. Particularly informative is current in the form of Gaussian white noise, which delivers a continuum of temporal frequencies in equal measure to reveal how they may be differentially propagated by the cell. Temporal frequency is important because continuous eye movements, together with motion in the scene, cause each cone to experience the visual image as a dynamic modulation of light intensity (Figures 1C and 1D; Rucci, 2008).

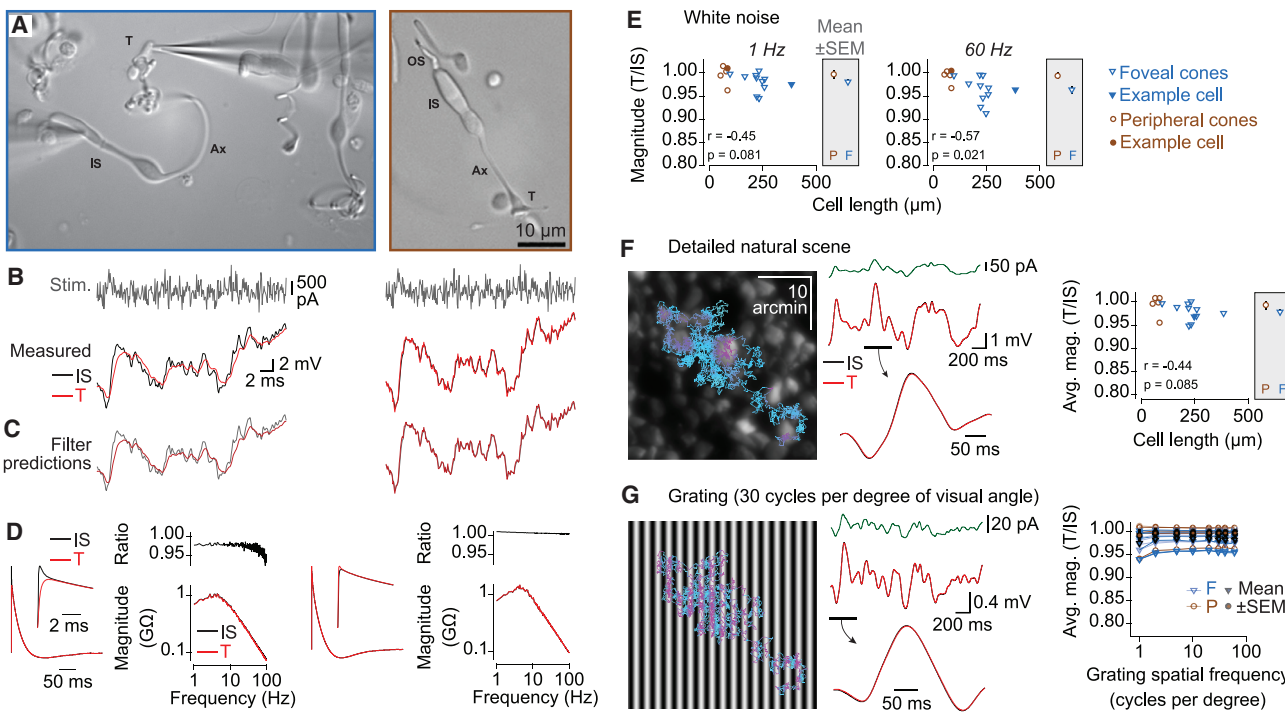


Figure 2. Foveal Cones Propagate Electrical Signals with High Fidelity

- (A) Dissociated foveal (left, with electrodes) and peripheral (right) cones. Axons of the former coil partially out of focus.
- (B) Assessing signal propagation in a dissociated foveal (left column) and peripheral (right) cone by stimulating the IS with current in the form of temporal white noise (stim.) and recording both IS and terminal voltage responses.
- (C) Linear filters summarize the current-to-voltage transformations at the IS and terminal. These filters accurately predict responses ($r = 0.96$ at each site for stimuli held out from filter construction; across cones, r values were 0.93–0.99).
- (D) Linear filters for the IS (black) and terminal (red), shown in the time domain (left; normalized to IS peak) and frequency domain (right). The magnitude at the terminal relative to that at the IS (terminal/IS ratio) is also shown.
- (E) Terminal/IS magnitude ratio (as in D) as a function of cell length (between recording sites). Shown are example low and high temporal frequencies (1 Hz and 60 Hz; the latter being a common refresh rate for video displays and corresponding to a point where the IS response magnitude is declining steeply, as shown in D). Detailed statistics for all scatterplots are in [Table S1](#).
- (F) Naturalistic phototransduction current (green), simulated for viewing of a detailed scene (as in [Figure 1C](#)), produces IS (black) and terminal (red) responses based on measured linear filters. Example uses IS and terminal linear filters measured from the foveal cone exhibiting the most response attenuation at 60 Hz (E). Group data show the terminal/IS magnitude ratio for each pair of IS and terminal linear filters, weighted by the photocurrent magnitude at each frequency and then averaged across frequencies.
- (G) Same type of simulation and analysis as (F) but with the natural scene substituted by gratings of various spatial frequencies in the visible range. Shown on left is the simulation for a 30 cycles per degree grating.

In foveal cones, the response at the terminal was marginally smaller and slower than that at the IS ([Figure 2B](#)), contradicting the expectation of poor propagation ([Figures 1D](#) and [1E](#)). In peripheral cones, responses at the two sites were nearly identical ([Figure 2B](#)). Following convention, we quantify the current-to-voltage relations of the terminal and IS as temporal filters, which accurately predict responses to arbitrary stimuli ([Figures 2C](#) and [S2](#); [Baccus and Meister, 2002](#); [Kim and Rieke, 2001](#)). Our measure of propagation fidelity is the ratio of terminal and IS filter magnitudes across temporal frequency. We display frequencies from 1 to 100 Hz, spanning the rate at which static retinal images tend to fade from perception and the rate at which temporal flicker appears continuous to foveal vision ([Figure 2D](#); [Coppola and Purves, 1996](#); [Rovamo et al., 1999](#)). Even for high temporal frequencies in the longest cones examined, where attenuation should be steepest, the terminal:IS magnitude ratio is >0.90 ([Figure](#)

[2E](#); see [Figures 4, 6](#), and [8](#) for additional information on the dependence of propagation on cell length). Propagation fidelity is also high for the relative timing of terminal and IS responses and for responses elicited with diverse stimuli ([Figure S2](#); terminal/IS ratios for phase lag are also near 1 and are provided in [Table S1](#)). The propagating responses of most cones are likely to change by <10% under conditions of natural viewing, even for the high spatial frequencies found in detailed images ([Figures 2F](#) and [2G](#)). Hence, our experiments reveal that all primate cones propagate signals with high fidelity—even the extreme length and slenderness of foveal cones does not impede the flow of visual information.

High-Fidelity Signal Propagation without Amplification

A common mechanism of signal propagation is the production of regenerative spikes by voltage-gated ion channels. We

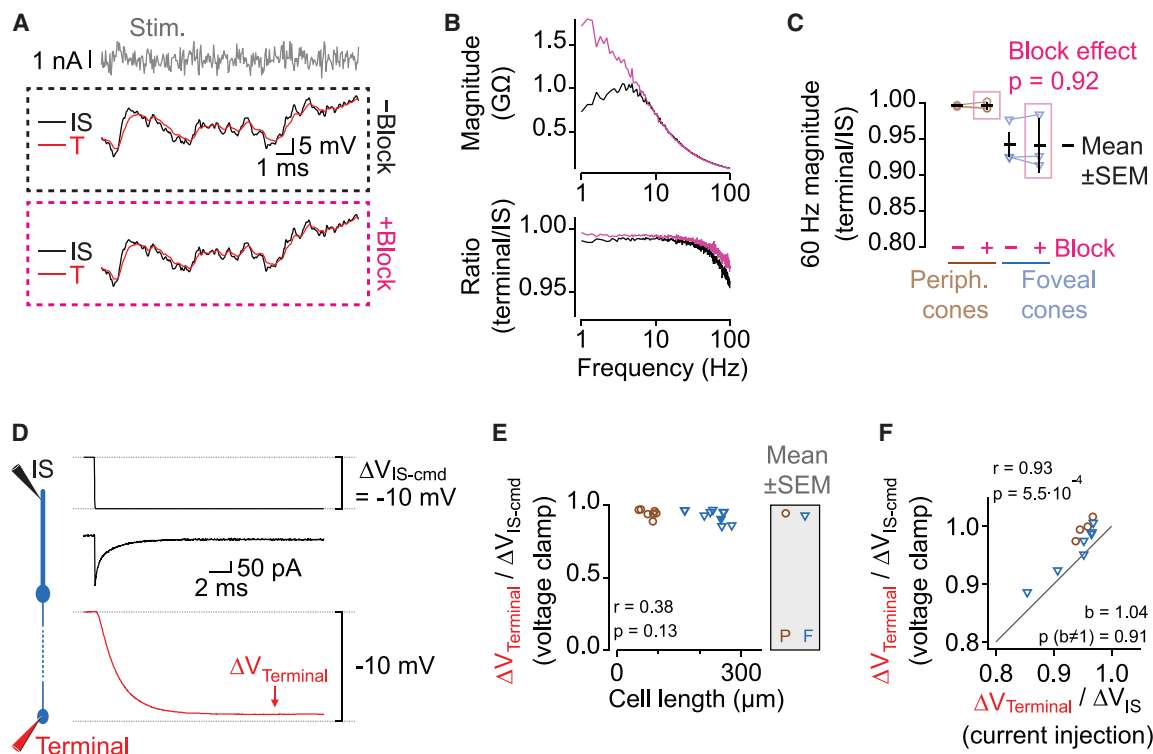


Figure 3. High-Fidelity Signal Propagation without Amplification

(A) Top: excerpt of the white-noise current stimulus (stim.) delivered to the inner segment (IS) of a dissociated foveal cone. IS and terminal (T) voltage responses are overlaid below, without and with block of all voltage-gated ion channels (Figure S3). The blockers solution was (in mM) 23.8 NaCl, 3.6 KCl, 1.2 MgCl₂, 6 glucose, 22.6 NaHCO₃, 0.0001 tetrodotoxin, 10 CsCl, 2 CoCl₂, 80 tetraethylammonium-Cl, and 10 4-aminopyridine.

(B) Top: response magnitude at the IS with channels free or blocked for the example cone. Bottom: terminal/IS magnitude ratios with channels free or blocked are shown.

(C) Terminal/IS magnitude ratios (at 60 Hz) without and with block across dissociated cones. Detailed statistics for multiple comparisons tests are in Table S2.

(D) A voltage command at the IS (ΔV_{IS-cmd} , at top; resultant capacitance transient in middle) effectively propagates to the terminal (voltage at bottom). Figure S4 provides evidence that the voltage change is passive (i.e., unamplified by voltage-gated ion channels). Traces are the average of 12 trials.

(E) The ratio of terminal voltage change (averaged in a time window at steady state) and IS voltage command ($\Delta V_{Terminal} / \Delta V_{IS-cmd}$) is near unity across dissociated cones. A smaller ratio would reflect a lower fidelity of propagation.

(F) $\Delta V_{Terminal} / \Delta V_{IS-cmd}$ compared to $\Delta V_{Terminal} / \Delta V_{IS}$. The latter was obtained during injection of current steps at the IS (Figure S2D, middle), where voltage-gated ion channels are free to support propagation. Line has unit slope; the slope from linear regression (b) is close to unity, indicating that voltage-gated channels contribute little to propagation even when they are free to do so. A divergence from unity would have indicated that voltage-gated channels contribute to the effective propagation observed in Figures 2 and S2.

never observed spikes during stimulation with white noise (0 of 17 foveal and peripheral cones). A single, broad spike was sometimes elicited by the injection of stepwise currents (8 of 16 foveal and peripheral cones tested; Figure S2A). These results are consistent with the understanding that cones communicate predominantly with graded voltages (Van Hook et al., 2019).

To ask whether the graded responses of primate cones are actively amplified during propagation (Carter et al., 2012), we blocked all voltage-gated ion channels with antagonists (Figure S3). Injecting white-noise current into the IS and measuring voltage at the IS and terminal allowed us to examine propagation with and without block in the same cell (Figure 3A). Blocking voltage-gated channels altered features of the response, changing its temporal frequency tuning from band-pass to low-pass (Figure 3B). Nevertheless, the terminal response remained a

faithful reflection of that in the IS (Figures 3B and 3C; Table S2). Active amplification appears to be dispensable for high-fidelity signal propagation.

Block of voltage-gated channels raises input resistance (Figure S3C) and may artificially boost propagation as a consequence. Thus, we conducted complementary experiments in solutions that lacked antagonists, where input resistance remained at its physiological level. We eliminated the effect of voltage-gated channel activity in this condition by clamping the IS voltage (Figure 3D). Voltage steps imposed on the IS evoked responses at the IS and terminal that both scaled linearly with the magnitude and polarity of the steps (Figure S4). Because voltage-gated currents are nonlinear (e.g., Figures S2, S3A, and S7), this linearity indicates that the effect of voltage-gated channel activity was nullified throughout the cell. Even so, propagation fidelity appeared undiminished: the magnitude of the

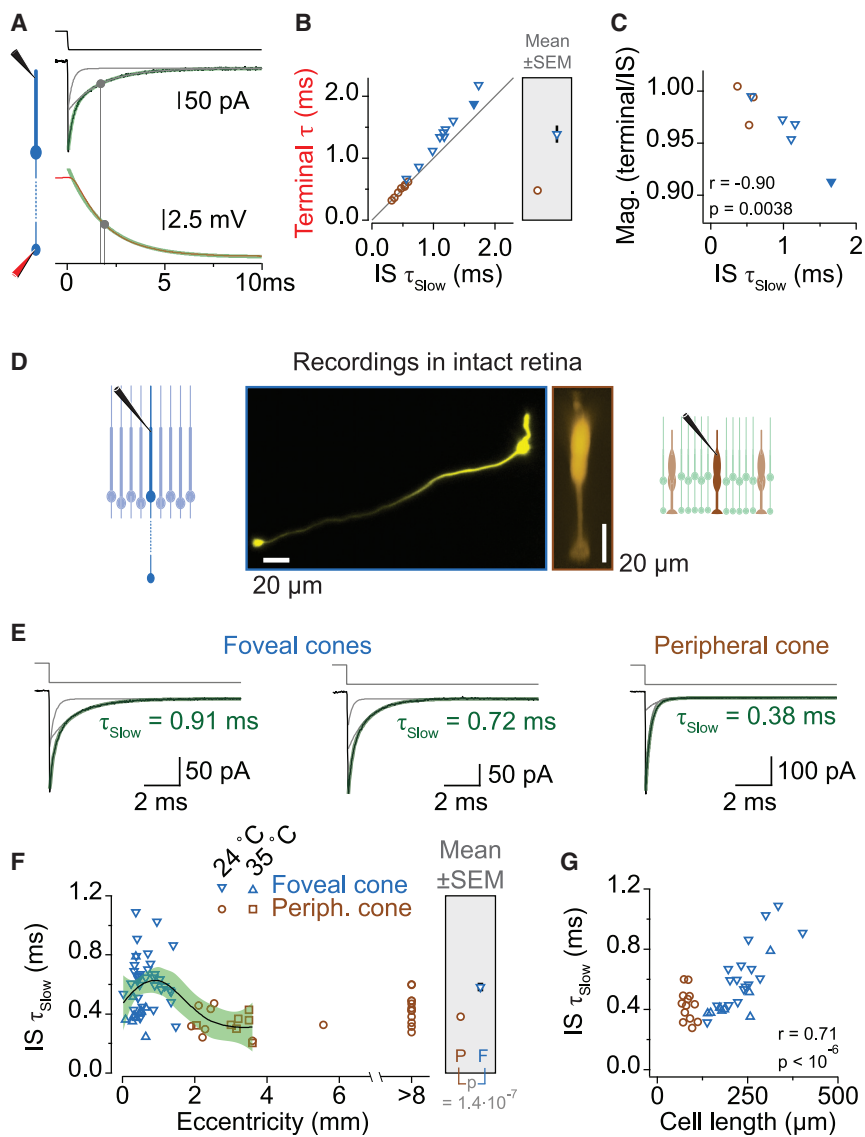


Figure 4. High-Fidelity Signal Propagation within the Primate Retina

(A) A voltage command delivered at the IS (top) produces a capacitance transient (middle) and change in terminal voltage (bottom). Responses are fit with exponentials (green; the sum of two components for the IS capacitance transient, with the components shown in gray, and one exponential for the terminal τ). The fast component of the IS capacitance transient reflects charging of the cellular regions near the electrode, and the slow component (IS τ_{Slow}) reflects charging of more distal regions. Vertical lines indicate the similar values of IS τ_{Slow} and terminal τ in this example cell; their similarity indicates that IS τ_{Slow} can be used as a proxy for terminal charging. Same traces as in Figure 3D are shown.

(B) Across dissociated cones, the slow time constant of the IS capacitance transient (IS τ_{Slow}) closely matches terminal τ . Filled symbol represents the example cell in (A).

(C) IS τ_{Slow} predicts terminal/IS response magnitude (mag.) measured with white noise currents (and phase with $r = 0.98$; Table S1). This correlation holds across temporal frequencies (the magnitude at 60 Hz is shown). Filled symbol represents the example cell in (A).

(D) Confocal projections of foveal (left) and peripheral (right) cones recorded in the retina.

(E) Voltage steps (top) and the resulting IS capacitance transients (bottom) recorded at the IS of the pictured foveal cone (left), a foveal cone recorded near physiological temperature (center), and the pictured peripheral cone (right). Traces are the average of 144, 40, and 32 trials (from left to right).

(F) IS τ_{Slow} as a function of eccentricity (distance from foveal center). IS τ_{Slow} is consistently rapid, indicating high-fidelity signal propagation across foveal and peripheral cones. Line is locally estimated scatterplot smoothing (LOESS) regression ($\pm 95\%$ confidence interval). The peak of the relation occurred at 0.92 mm eccentricity (with a 95% confidence interval of 0.38–1.3 mm), where τ_{Slow} was 0.63 ms (0.54–0.72). At eccentricities of 0.2 and 3 mm, τ_{Slow} was 0.53 ms (0.44–0.65) and 0.31 ms (0.26–0.37), respectively.

(G) As in (F) but for cell length. Data shown are directly comparable to Figure S5B, concerning dissociated cones.

terminal voltage change was nearly equal to that of the IS voltage step (Figure 3D). This match held across cones of different lengths (Figure 3E). Moreover, it was similar to that found when channels were free to contribute to propagation (i.e., when current was injected into the IS and voltage monitored at both locations; Figures 3F and S2D). From these results, we conclude that passive properties endow primate cones with high-fidelity signal propagation.

High-Fidelity Signal Propagation through Cones within the Retina

We sought to evaluate passive propagation through cones that are embedded in retinal circuitry. Their terminals are inaccessible for electrophysiological recording, but experiments on dissociated cones indicate that propagation fidelity can be moni-

tored through the IS response alone. A stepwise change in voltage delivered at the IS produces a capacitance transient, which is the current that charges the cell membrane to the new voltage (Figure 4A). The relaxation of this transient is well described by the sum of two exponentials (Figures 4A and S5). The fast exponential reflects the rapid charging of membrane that is proximal to the IS pipette, where current is injected for voltage clamp. The slower exponential (τ_{Slow}) reflects the more gradual charging of distal membrane. At the terminal, the voltage follows a single exponential (terminal τ) because it primarily reflects one process, the accumulation of charge that reaches this site (Figure 4A; further analysis in Figure S5). IS τ_{Slow} is nearly identical to terminal τ across cones (Figure 4B) and predicts the fidelity of propagation (Figure 4C). We therefore used IS τ_{Slow} to gauge the effectiveness of terminal charging for cones recorded

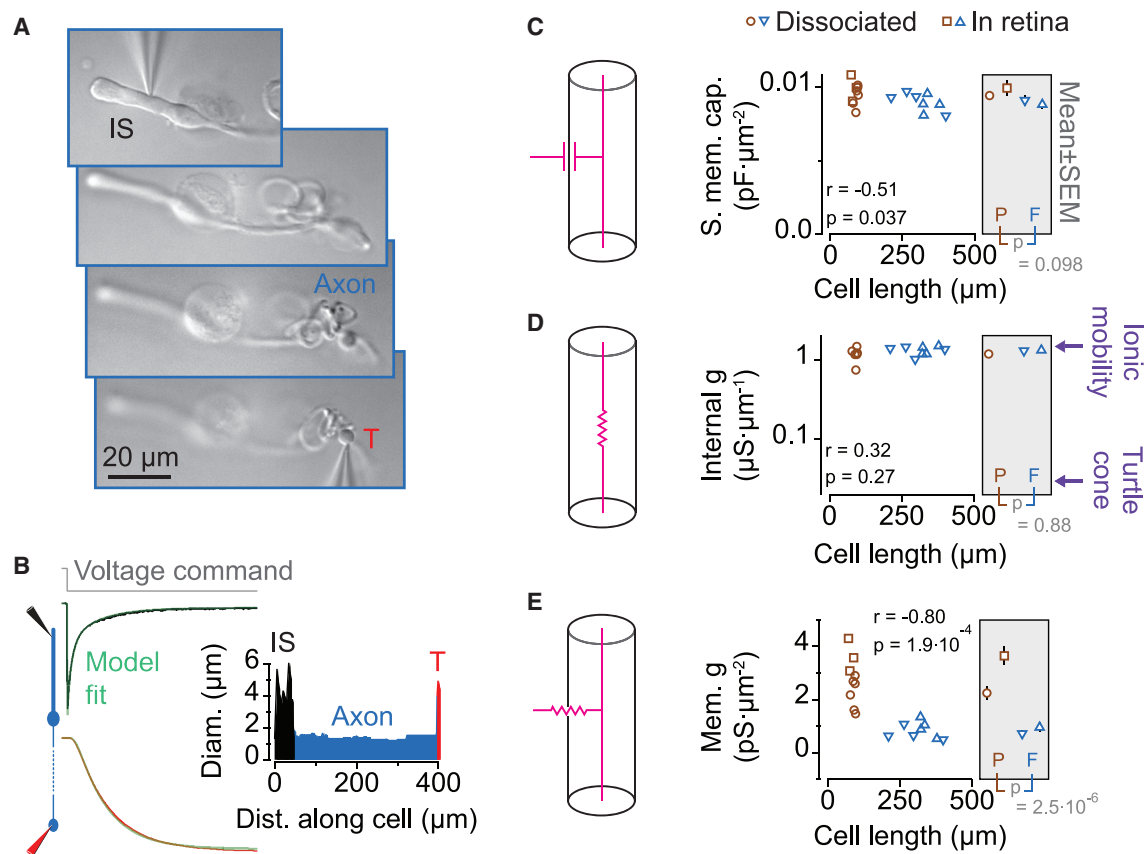


Figure 5. Biophysical Mechanisms of High-Fidelity Signal Propagation

(A) Example of a dissociated foveal cone that was imaged for morphological reconstruction and passive compartmental circuit modeling. Shown is a subset of the focal planes used for reconstruction.

(B) Left: measured responses at the IS (black) and terminal (red) overlaid with model fits (green) for the cell in (A). Right: quantification of morphology for the same cell is shown. Traces are the average of 16 trials. Pearson correlation coefficient (r) value was 0.996 for this circuit model and similarly high for all other cells. (C–E) The biophysical properties that govern signal propagation through primate cones, obtained from model fits to data and plotted against cell length: specific membrane capacitance (s. mem. cap.; C), internal conductivity (internal g ; D), and membrane conductivity (mem. g ; E). An axonal length constant can be calculated using the mean biophysical parameters ($s_{\text{mem cap}} = 0.01 \text{ pF} \cdot \mu\text{m}^{-2}$; internal $g = 1.3 \mu\text{S} \cdot \mu\text{m}^{-1}$; mem $g = 0.83 \text{ pS} \cdot \mu\text{m}^{-2}$), a constant diameter of $1.6 \mu\text{m}$, and the simplifying assumption of a semi-infinite cable. The resulting value is $791 \mu\text{m}$, almost double the length of the longest foveal cone axons. See STAR Methods for additional details. The lower membrane conductivity of dissociated cones is expected from the lack of gap junctions in this condition; in the retina, gap junctions also appear to have a larger effect on peripheral than foveal cones (Sinha et al., 2017).

only at the IS in the intact retina (Figure 4D; see STAR Methods for further discussion).

Terminal charging of cones recorded in the retina appeared fast (τ_{slow} of $0.2\text{--}1.1 \text{ ms}$ across 27 peripheral and 45 foveal cones; Figures 4E–4G) and similar to that of dissociated cones (compare with Figure S5B). Close examination reveals that terminal charging tends to be rapid in the central fovea, slower just beyond, and most rapid in the periphery (Figure 4F); this pattern broadly follows the non-monotonic variation in cone length that we (Figure 4G) and others (Drasdo et al., 2007; Perry and Cowey, 1988) have observed. These experiments indicate that propagation, being similar whether cones are dissociated or embedded in the retina, is independent of factors like ensheathment by glial processes (contrary to prior expectations; Perry, 1990), extracellular resistance, and the presence of an OS (further analysis in Figure S6).

Biophysical Optimizations for High-Fidelity Propagation

Three biophysical properties govern the passive propagation of electrical signals through a cell: specific membrane capacitance (the charge needed to alter the voltage of a unit area of membrane); membrane conductivity (how readily current flows through the membrane and is lost to extracellular space); and internal conductivity (how easily current flows within the cell and is therefore conveyed across compartments; Rall et al., 1992). We extracted these properties from circuit models (Carnevale and Hines, 2009) built according to the measured morphologies and passive electrical responses of cones (Figure 5). These models accurately captured IS and terminal responses (Figure 5B). They yielded biophysical parameters that were robust to experimental conditions. The parameters were similar for recordings with different series resistances (Table S1). They were also similar for cones recorded in the retina and after dissociation

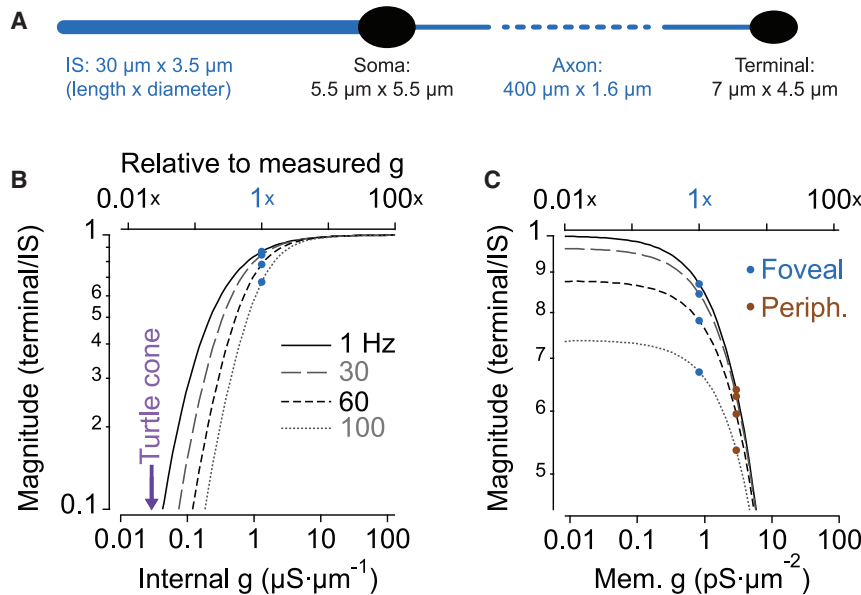


Figure 6. The Biophysical Mechanisms of Foveal Cones Are Optimized for High-Fidelity Propagation

(A) Schematic illustrating the reference foveal cone, which was designed to be among the longest and most slender observed. This reference cone was used in computational simulations that examined how the fidelity of propagation changed as biophysical properties were varied from their natural values (see Figure 5).

(B) Computational simulation indicates that the natural value (blue dots) of internal conductivity (g) is nearly optimal for propagation fidelity.

(C) Same plot for membrane (mem.) conductivity. As with internal conductivity, changing this parameter more readily degrades than improves fidelity. Propagation fidelity is highlighted for the natural value of membrane conductivity for foveal cones (blue dots) and for the hypothetical situation where the membrane conductivity of peripheral cones is substituted (brown dots).

(providing additional evidence that the normal environment contributes negligible capacitance or resistance; Figures 5C–5E). The specific membrane capacitance of all cones was near 0.01 $\text{pF}\cdot\mu\text{m}^{-2}$ (Figure 5C; equivalent to $1 \mu\text{F}\cdot\text{cm}^{-2}$), which is typical across cell types (Rall et al., 1992). By contrast, the internal conductivity was exceptionally high ($1.3 \mu\text{S}\cdot\mu\text{m}^{-1}$; Figure 5D; equivalent to $80 \Omega\cdot\text{cm}$). This conductivity is ~ 40 -fold greater than the estimate for turtle cones ($0.03 \mu\text{S}\cdot\mu\text{m}^{-1}$; Lasater et al., 1989) and approaches that of saline ($\sim 1.5 \mu\text{S}\cdot\mu\text{m}^{-1}$). Foveal and peripheral cones diverged in their membrane conductivity. It was ~ 3.5 -fold lower in the former (Figure 5E). High internal conductivity and low membrane conductivity are expected to facilitate current flow within, but not out of, cells. Thus, we hypothesized that biophysical properties are not just distinct in foveal cones but tuned to values that optimize propagation through these elongated cells.

To test for optimality, we systematically varied internal and membrane conductivities within a modeled foveal cone and compared responses at the IS and terminal. We designed this reference cone to be among the longest and most slender that we and others have measured (Figure 6A; Curcio et al., 1990; Drasdo et al., 2007; Hsu et al., 1998; Perry and Cowey, 1988). Initialized with the mean biophysical parameters that we obtained for foveal cones, the reference cone displayed high-fidelity propagation (see blue dots in Figures 6B and 6C). Artificially decreasing internal conductivity caused a steep reduction in fidelity (i.e., response magnitude at the terminal diverged from that at the IS; Figure 6B). Increasing membrane conductivity had a similar effect; substituting the higher value of peripheral cones reduced fidelity by a third (at 60 Hz; Figure 6C). In addition, it appears that propagation can hardly be improved. Internal conductivity already appears ideal, approaching that of free saline (Figure 5D). Moreover, decreasing membrane conductivity by 100-fold produced little improvement (e.g., changing the terminal/IS ratio from 0.78 to 0.87 at 60 Hz; Figure 6C). Achieving even this small improvement seems impractical. For example, blocking all voltage-gated ion channels only halved input

conductance (Figure S3C). This manipulation did not alter fidelity (Figures 3A–3C), even as it caused qualitative changes to the cellular response (Figure 3B). Collectively, these analyses indicate that the biophysical properties of foveal cones are essentially optimal for high-fidelity signal propagation.

The Basis of Biophysical Optimization

What is the origin of these biophysical optimizations? Internal conductivity (and propagation fidelity) appeared to be unaffected by exchange of cytosol with electrode solution (Figures 7A and 7B), which had a standard composition (Kay, 1992). Accordingly, high internal conductivity is unlikely to arise from a specialization of the cytosolic composition, such as enrichment of especially mobile ions. Instead, it is likely due to ultrastructure. A prominent feature of cones is that mitochondria fill most of the volume of the IS. These organelles are bundled in parallel for primate cones (Dowling, 1965; Hoang et al., 2002). This organization has been unexplained but contrasts starkly with the enmeshed configuration of other species, which is likely to impede ionic diffusion (Giarmarco et al., 2017; Samorajski et al., 1966). Our findings suggest that the intracellular structures of foveal cones provide open pathways for current flow.

With regard to low membrane conductivity, the standard explanation is a lack of voltage-insensitive “leak” channels. However, the membrane conductance of primate cones showed a steep dependence on voltage that indicates a dominant contribution from voltage-gated ion channels (changing by 1.9- to 2.4-fold per 20 mV for a voltage range from -47 mV to -87 mV across 14 foveal and 16 peripheral cones recorded in the retina; Table S2). We considered the channels that mediate $I_{K\alpha}$ (a low-threshold K^+ current) and I_h (the hyperpolarization-activated cationic current; Gayet-Primo et al., 2018; Yagi and Macleish, 1994). In cones, these channels are stably activated over complementary voltages that span the physiological range (Barnes, 1994); hence, they are poised to set the steady membrane conductance. We found that both currents were larger in

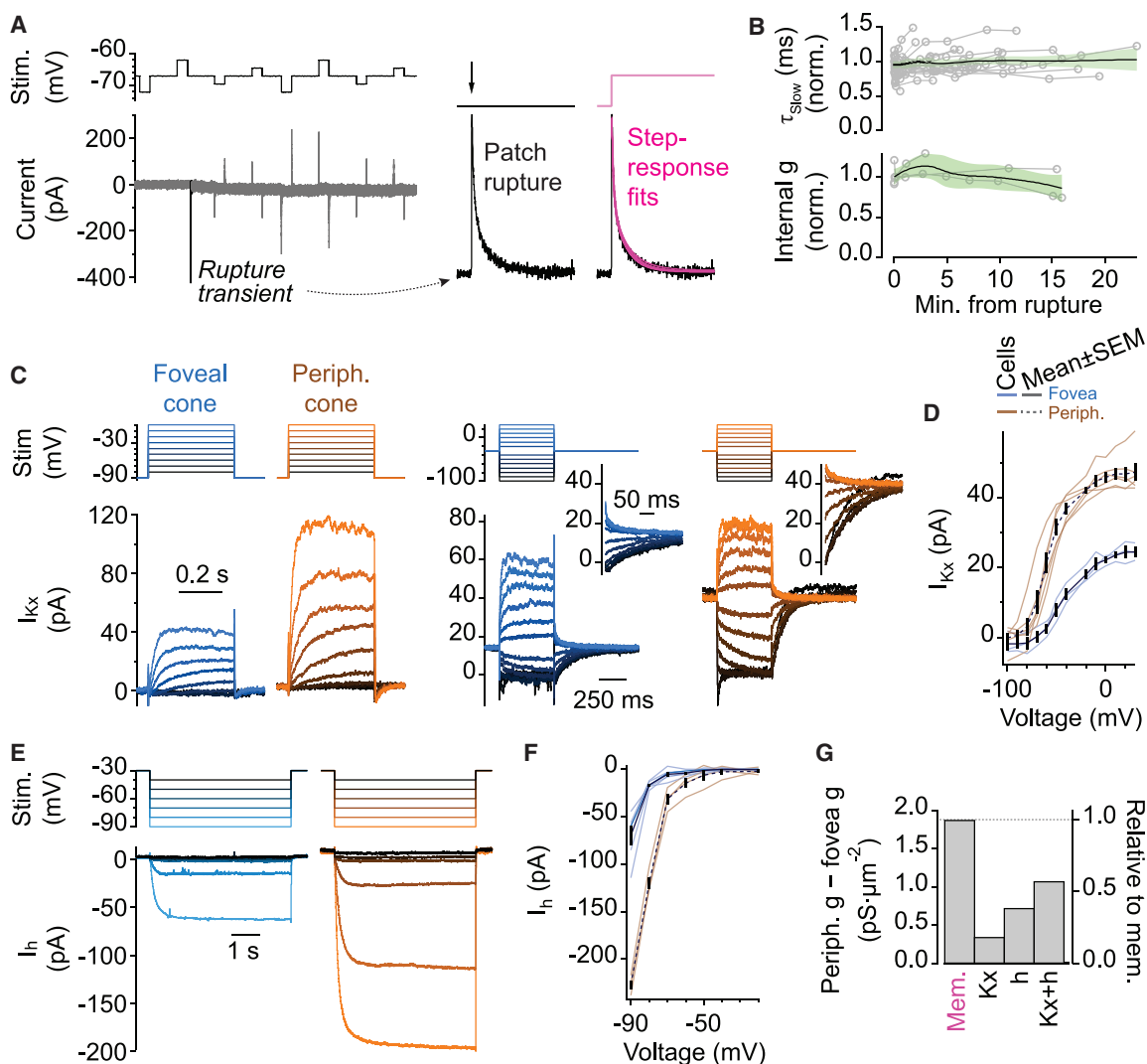


Figure 7. Origins of Biophysical Optimizations for High-Fidelity Signal Propagation

(A) Propagation fidelity appears unaffected by exchanging cytosol with electrode saline. (Left) Voltage clamp of the IS produced capacitance transients (bottom), shown for a foveal cone recorded in the retina. The first transient resulted from rupture of the membrane patch (black), which initiated voltage clamp and cytosolic exchange. This rupture transient is shown normalized (center) and overlaid with double-exponential fits of capacitance transients evoked by voltage steps (right; 8 time points over a ~10-min period after rupture).

(B) Slow exponential time constant (τ_{slow}) and internal conductance over time, relative to values at rupture. τ_{slow} from 19 foveal cones and 1 peripheral cone recorded in the retina are shown; a subset was suitable for estimating internal conductance. Lines, LOESS regression \pm 95% confidence interval.

(C) A principal hyperpolarizing current (I_{Kx}) of photoreceptors is smaller in foveal than peripheral cones. I_{Kx} was evoked by voltage steps (top) from a baseline voltage of -90 mV (left) or -30 mV (right) and isolated by pharmacological subtraction. Data from two example cones are shown. For isolation of I_{Kx} , the control solution contained (in mM) is 107 NaCl, 10 N-methyl-D-glucamine-Cl, 3 CsCl (to block I_h), 3.6 KCl, 1.2 CoCl₂ (substituted for CaCl₂ to suppress Ca²⁺ and Ca²⁺-activated currents), 1.2 MgCl₂, 6 glucose, and 22.6 NaHCO₃. I_{Kx} was blocked by replacement of N-methyl-D-glucamine-Cl with tetraethylammonium-Cl.

(D) Relation of steady I_{Kx} to voltage, measured from tail currents (as shown in the insets of C).

(E and F) A principal depolarizing current of photoreceptors (I_h), evoked by voltage steps from -30 mV and isolated by pharmacological subtraction. For isolation of I_h , the control solution contained (in mM) 117 NaCl, 3 N-methyl-D-glucamine-Cl, 3.6 KCl, 1.2 CaCl₂, 1.2 MgCl₂, 6 glucose, 22.6 NaHCO₃, and 0.3 BaCl₂; pH 7.2 with HCl. I_h was blocked by the replacement of N-methyl-D-glucamine-Cl with CsCl.

(G) The contribution of voltage-gated channels to membrane conductivity. The left axis gives the difference in membrane conductivity between foveal and peripheral cones. “Mem.” is the total difference, obtained from fitting passive compartmental models to measured responses (Figure 5E). “Kx” and “h” are the portions of that difference accounted for by channels that mediate I_{Kx} and I_h . These values are calculated from the data in (D) (for Kx) and (F) (for h) as described in STAR Methods. The right axis shows the normalized differences in membrane conductivities. I_{Kx} and I_h channels account for ~60% of the higher total membrane conductivity of peripheral cones.

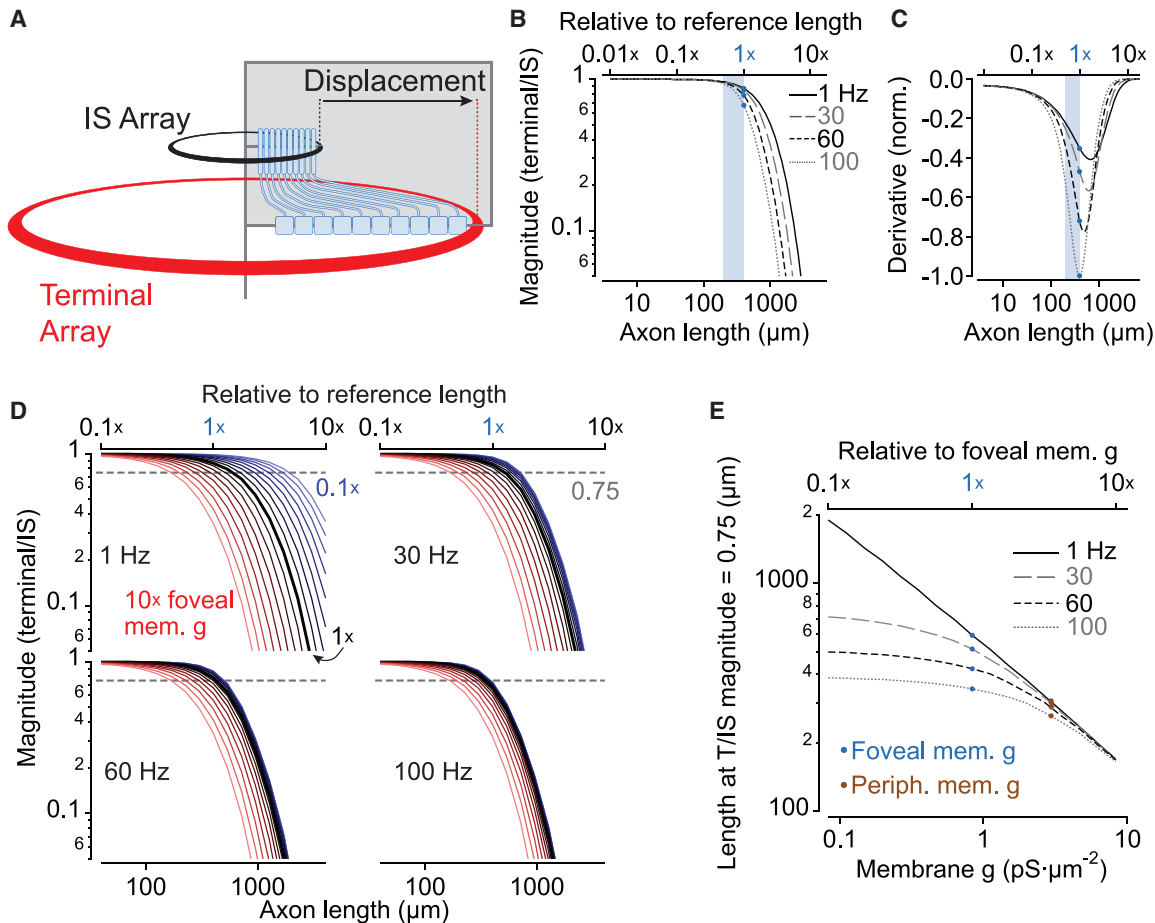


Figure 8. Biophysical Constraints on Foveal Size

- (A) Foveal cone terminals are larger than inner segments (ISs). Increasing the number of cones to expand the fovea causes progressively greater displacement of terminals from ISs, necessitating longer axons (Schein, 1988).
- (B) Assessing whether the specialized biophysical properties of foveal cones can support longer axons while maintaining propagation fidelity. Plot shows response magnitude ratio (terminal/IS) for various temporal frequencies as axon length is varied. Blue dots indicate the length of the reference foveal cone. Blue bar indicates axon lengths of foveal cones for which passive properties were determined (Figures 5C–5E).
- (C) First derivatives of curves in (B) (normalized to the peak of the 100-Hz relation). Propagation fidelity declines most steeply at the upper limit of natural axon lengths.
- (D) Decreasing membrane conductivity (mem. g) cannot preserve fidelity for longer axons except at low frequencies. Thick black lines show relations for measured foveal membrane conductivity (same as in B). Other lines are for 0.1- to 10-fold variations. Dotted line indicates a fixed magnitude ratio of 0.75, used for quantification in (E).
- (E) Decreasing membrane conductivity allows only slightly longer axons except at low frequency (e.g., 1 Hz).

peripheral than foveal cones (Figures 7C–7F and S7). They account for most of the difference in membrane conductance between these cells (Figure 7G). Thus, although voltage-gated ion channels support long-distance communication in other neurons, their scarcity does in foveal cones.

Biophysical Constraints on Foveal Size

We asked whether the biophysical properties of foveal cones, being well-tuned for signal propagation, could support longer axons and thus a larger fovea and more expansive high-acuity visual field. Axon length is linked to foveal size because the IS monolayer is denser than the terminal monolayer; increasing IS number (to expand the fovea) would necessitate a greater

displacement of downstream terminals and thus longer axons (Figure 8A; Schein, 1988). We found that elongating the axon of the reference foveal cone model (see above) caused fidelity to fall. This drop was steepest near the upper limit of axon lengths found in nature (Figures 8B and 8C). In principle, an even lower density of ion channels in foveal cones could support propagation through longer axons. However, reducing the membrane conductivity only improved propagation of low frequencies (Figures 8D and 8E) because the hypothetical cone acted as an extended series of strong low-pass filters. To summarize, foveal cones appear confined to lengths for which their electrical architecture can support high-fidelity signal propagation. This biophysical constraint provides a new explanation

for why the fovea is a minuscule portion of the entire retina (<1%) and why its absolute size is conserved even as the retinal surface area varies several-fold from marmosets to humans (Franco et al., 2000).

DISCUSSION

Biophysical mechanisms endow some primate neurons with properties that their counterparts in other species lack (Beaulieu-Laroche et al., 2018; Eyal et al., 2016; Gidon et al., 2020). How these properties relate to the specific capabilities of primates has been an open question. We provide an answer in the foveal cones. These neurons use biophysical mechanisms that are tuned differently from those of cones outside the fovea and in other species. This tuning allows foveal cones to propagate signals with high fidelity, consistent with the extraordinarily sharp vision of primates. These mechanisms provide explanations for structural features of foveal cones, and their constraints suggest why the fovea itself has a limited size. Here, we add context to these findings and highlight open questions.

High-Fidelity Signal Propagation through Foveal Cones

Prior knowledge of photoreceptor biophysics suggests that foveal cones attenuate visual signals as they flow from their origin in the outer segment to the presynaptic terminal (Hsu et al., 1998; Lasater et al., 1989), to a degree that appears unsuited to modulating neurotransmitter release (Figure 1). The slowness of foveal phototransduction has been explained in this framework, because low frequencies are generally less prone to attenuation (Masland, 2017; Sinha et al., 2017). In addition, the close association of glial cells and foveal cones has been proposed to aid propagation by providing insulation (Perry, 1990). However, prior to the experiments described here, neither propagation nor its biophysical underpinnings had been measured in foveal cones. The only measurements from vertebrate photoreceptors, done on turtle cones, estimated an internal conductivity that would cause severe attenuation (Lasater et al., 1989). Electrophysiological recordings from the long photoreceptors of barnacles found that propagating signals were distorted despite a low membrane conductivity (Hudspeth et al., 1977) and some amplification by voltage-gated currents (Edgington and Stuart, 1979). Our work on primate foveal cones reveals a flow of visual information that is essentially lossless and that arises from intrinsic, passive mechanisms. An implication is that foveal phototransduction kinetics and neuroglial interactions are likely to serve other purposes, which remain to be determined. Effective propagation may be particularly important in the fovea—each output neuron is driven almost entirely by one cone and thus depends on the signal quality within a single presynaptic terminal for its own response fidelity.

The Origins of Biophysical Optimization in Foveal Cones

We have found that the high fidelity of signal propagation through foveal cones is supported by two biophysical mechanisms. One is a high internal conductivity. This feature is shared with peripheral cones and allows current to flow freely throughout the cell. We propose that high internal conductivity is due to the arrangement of organelles and cytoskeleton within primate cones.

Testing this proposal will require high-resolution, three-dimensional reconstructions of whole cells that retain natural intracellular volumes (Hoffman et al., 2020; Pallotto et al., 2015; Volland and Williams, 2018). Such reconstructions would provide the basis for modeling ionic diffusion through small compartments, an emerging field (Holcman and Yuste, 2015; Savchenko et al., 2017). Ultrastructural specializations are likely to exist. As mentioned above, columnar bundles of mitochondria may provide channels for ionic conduction through primate cones (Dowling, 1965; Hoang et al., 2002). Similar bundles are found in squirrel cones but, intriguingly, are less ordered when the animals hibernate (Sajdak et al., 2019). Perhaps maintaining this organization is metabolically demanding. Such a demand may be met more readily by peripheral than foveal cones, given that the latter have fewer mitochondria and dwell in an avascular zone (Hoang et al., 2002; Yu et al., 2005). The metabolic requirements of foveal cones may help explain why certain diseases target the fovea—for example, macular degeneration, a leading cause of blindness.

Foveal cones diverge from peripheral cones in having a low membrane conductivity, which reduces loss of current to extracellular space. Our observations suggest that most of this lower conductivity is explained by a lower density of $I_{K\alpha}$ and I_h . The difference arises in part from properties of the underlying ion channels; we found that $I_{K\alpha}$ activates at a more depolarized potential in foveal cones (Figure S7F), which limits its size in the physiological range. Our observations are also consistent with differences in the expression levels of channels mediating $I_{K\alpha}$ and I_h , as both currents were smaller in foveal cones across all voltages tested. We have not detected a difference in transcript abundance (Peng et al., 2019), suggesting the importance of translational or post-translational regulation. Investigating these regulatory mechanisms would provide further insight into how the functional properties of primate cones are diversified according to behavioral needs.

The Uniqueness of Vision and Foveal Cones in Primates

The spatial acuity of vision in humans and other primates is the highest among mammals, surpassing that of cats by ~10-fold and mice by ~100-fold (Harmening et al., 2009). Across the animal kingdom, only certain raptors exceed this performance, though they require ~10-fold greater contrast to discern a given level of detail (Mitkus et al., 2018). These raptors resemble primates in possessing foveas and therefore provide a useful comparison. Studies of the avian fovea are scarce but indicate that cone axons are short and do not form a distinct layer in the retina (Finlay et al., 2005; Lockhart, 1976; Mitkus et al., 2017; Reymond, 1985; Walls, 1942). These observations imply that the presynaptic terminals of avian foveal cones are small; primate foveal cones extend long axons because their array of large terminals is wider than that of their smaller inner segments (Schein, 1988). A larger presynaptic terminal has the potential to sustain a higher maximum rate of neurotransmitter release and allow even subtle changes in brightness to evoke sizeable modulations in rate (provided that responses propagate effectively to the terminal). In other words, large terminals are suited for contrast enhancement, which could help to explain the higher contrast sensitivity of primates. Future work may test these ideas.

and perhaps uncover specializations in the coupling of propagated signals to the machinery of synaptic release.

Biophysical Limits to Foveal Size

The fovea occupies a tiny fraction of the retina and is scanned across space to produce the experience of a seamlessly detailed visual world. A larger fovea would seem advantageous, allowing detail to be extracted from more of the scene at each instant. However, fovea size is constant from marmosets to humans, species that differ in retinal surface area by ~5-fold, body mass by ~10-fold, and brain mass by ~150-fold (Franco et al., 2000; Herculano-Houzel et al., 2007). It has been speculated that foveal size is limited by the length of foveal cones (Franco et al., 2000). Indeed, our work indicates that propagation fidelity would fall precipitously if cones were extended beyond the lengths found in nature. We suggest that the requirement for fidelity has kept the fovea minuscule over primate evolution, alongside constraints like the already enlarged borders of foveal representations in the optic nerve and downstream brain regions (Polyak, 1941; Rodieck, 1998; Van Essen et al., 1984) and the high metabolic demands of neurons (Niven and Laughlin, 2008).

How much can fidelity fall before vision suffers? Addressing this question requires new investigations—for example, to define the nature of noise and its propagation relative to signal and the parameters of synaptic release (Angueyra and Rieke, 2013; Rao et al., 1994). Progress along these lines would allow a more rigorous comparison of performance between foveal cones and central vision. This comparison would foster understanding of how the distinct properties of foveal cones, previously reported for phototransduction (Sinha et al., 2017) and now for propagation, underlie the extraordinary spatial acuity and contrast sensitivity of primate vision.

In principle, amplification could preserve signals as they propagated through longer foveal cones. One drawback to amplification is energetic cost (Niven and Laughlin, 2008). Cones are already expensive due to the requirements of phototransduction (Okawa et al., 2008). Additional costs may be difficult to pay due to the aforementioned paucity of foveal mitochondria and vasculature. Other potential drawbacks are that channels contribute noise and require time to gate (White et al., 2000). Moreover, amplification might further differentiate the outputs of foveal and peripheral cones. In the extreme case, the former would produce regenerative potentials, which may carry less visual information (de Ruyter van Steveninck and Laughlin, 1996) and necessitate different modes of signal processing in downstream circuits.

An alternative to amplification is a further enhancement of passive properties. We found that internal conductivity already approaches that of ionic mobility in saline, suggesting little room for improvement. Internal conductance could be increased by widening the cell. Doing so for the inner segment is undesirable because it would broaden the receptive field and thus degrade spatial acuity. Expanding the axon also provides little gain; our simulations indicate that the increased conductance is counterbalanced by an increased capacitance that leaves propagation fidelity largely unchanged (not shown). With regard to membrane conductivity, reducing this parameter is unlikely to help. Blocking all voltage-gated ion channels only halved mem-

brane conductivity and had little effect on propagation fidelity. We have found that steeper reductions in membrane conductivity would only rescue propagation of low frequencies.

Taken together, these considerations suggest that the biophysical mechanisms of foveal cones are already optimized for signal propagation, placing a limit on cell length and thus foveal size. One avenue of future research is to ask how biophysical constraints have shaped the evolution of other neural tissues, such as the large human cortex and its functionally specialized neurons (Beaulieu-Laroche et al., 2018; Eyal et al., 2016; Gidon et al., 2020).

STAR★METHODS

Detailed methods are provided in the online version of this paper and include the following:

- KEY RESOURCES TABLE
- RESOURCE AVAILABILITY
 - Lead Contact
 - Materials Availability
 - Data and Code Availability
- EXPERIMENTAL MODEL AND SUBJECT DETAILS
- METHOD DETAILS
 - Tissue collection
 - Solutions
 - Tissue culture and microdissection
 - Electrophysiological recordings
 - Electrical stimulation
 - Estimating terminal charging from IS responses
 - Voltage-gated current analysis
 - Visual stimulation
 - Staining and immunohistochemistry
 - Imaging cellular morphology
 - Analysis of morphology
 - Electrical circuit models
 - Length constant
 - Natural image model
- QUANTIFICATION AND STATISTICAL ANALYSIS

SUPPLEMENTAL INFORMATION

Supplemental Information can be found online at <https://doi.org/10.1016/j.neuron.2020.07.035>.

ACKNOWLEDGMENTS

We are grateful to Richard Born for helping to establish our research program on macaque tissue and to Fred Rieke and Raunak Sinha for key methodological insights. We thank John Assad, Richard Born, Curtis Cetruleo, Jim DiCarlo, April Hall, R. Paul Johnsen, Margaret Livingstone, Joren Madsen, Tara Moore, Mark Nedelman, Mikhail Papisov, Douglas Rosene, and Stephanie Smith for generously providing tissue; Bruce Bean, Richard Born, Ulrike Grünert, Michael Hines, and Richard Masland for discussions; and laboratory members (Hannah Blume, Michael Brown, Alan Emanuel, Elliott Milner, and Philippe Morquette) for discussions and comments on the manuscript. Funding was provided by the BrightFocus Foundation (M2014055), the Lefler Center of Harvard Medical School, the Neurobiology Department of Harvard Medical School, the Harvard-MIT Joint Research Grants Program in Basic Neuroscience, the NIH (EY030628, EY025840, EY028633, and EY025555), and the National Science Foundation Graduate Research Fellowships Program. The NIH

also provided support through 1U54HD090255 (Boston Children's Hospital IDDRC) and P30 EY012196 (Harvard Medical School).

AUTHOR CONTRIBUTIONS

G.S.B. and M.T.H.D. conceived the study. G.S.B. designed, conducted, and analyzed experiments with guidance from M.T.H.D. G.S.B., A.L., and M.T.H.D. developed the logistical and technical framework for tissue procurement. G.S.B. and M.T.H.D. wrote the paper with input from A.L.

DECLARATION OF INTERESTS

M.T.H.D. is affiliated with the Center for Brain Science (Harvard University), the Division of Sleep Medicine (Brigham and Women's Hospital, Harvard Medical School), and the Broad Institute of MIT and Harvard. All authors declare no competing interests.

Received: March 30, 2020

Revised: June 24, 2020

Accepted: July 24, 2020

Published: August 25, 2020

SUPPORTING CITATIONS

The following references appear in the Supplemental Information: Chun et al. (1996); Cohen (1961).

REFERENCES

- Ambati, J., and Fowler, B.J. (2012). Mechanisms of age-related macular degeneration. *Neuron* 75, 26–39.
- Angueyra, J.M., and Rieke, F. (2013). Origin and effect of phototransduction noise in primate cone photoreceptors. *Nat. Neurosci.* 16, 1692–1700.
- Aytekin, M., Victor, J.D., and Rucci, M. (2014). The visual input to the retina during natural head-free fixation. *J. Neurosci.* 34, 12701–12715.
- Baccus, S.A., and Meister, M. (2002). Fast and slow contrast adaptation in retinal circuitry. *Neuron* 36, 909–919.
- Barnes, S. (1994). After transduction: response shaping and control of transmission by ion channels of the photoreceptor inner segments. *Neuroscience* 58, 447–459.
- Baylor, D.A., Nunn, B.J., and Schnapf, J.L. (1987). Spectral sensitivity of cones of the monkey *Macaca fascicularis*. *J. Physiol.* 390, 145–160.
- Beaulieu-Laroche, L., Toloza, E.H.S., van der Goes, M.-S., Lafourcade, M., Barnagian, D., Williams, Z.M., Eskandar, E.N., Frosch, M.P., Cash, S.S., and Harnett, M.T. (2018). Enhanced dendritic compartmentalization in human cortical neurons. *Cell* 175, 643–651.e14.
- Beech, D.J., and Barnes, S. (1989). Characterization of a voltage-gated K⁺ channel that accelerates the rod response to dim light. *Neuron* 3, 573–581.
- Biel, M., Wahl-Schott, C., Michalakis, S., and Zong, X. (2009). Hyperpolarization-activated cation channels: from genes to function. *Physiol. Rev.* 89, 847–885.
- Cao, L.H., Luo, D.G., and Yau, K.-W. (2014). Light responses of primate and other mammalian cones. *Proc. Natl. Acad. Sci. USA* 111, 2752–2757.
- Carnevale, N.T., and Hines, M.L. (2009). *The Neuron Book* (Cambridge University).
- Carter, B.C., Giessel, A.J., Sabatini, B.L., and Bean, B.P. (2012). Transient sodium current at subthreshold voltages: activation by EPSP waveforms. *Neuron* 75, 1081–1093.
- Caves, E.M., Brandley, N.C., and Johnsen, S. (2018). Visual acuity and the evolution of signals. *Trends Ecol. Evol.* 33, 358–372.
- Cavonius, C.R., and Robbins, D.O. (1973). Relationships between luminance and visual acuity in the rhesus monkey. *J. Physiol.* 232, 239–246.
- Chen, B., Makous, W., and Williams, D.R. (1993). Serial spatial filters in vision. *Vision Res.* 33, 413–427.
- Chun, M.H., Grünert, U., Martin, P.R., and Wässle, H. (1996). The synaptic complex of cones in the fovea and in the periphery of the macaque monkey retina. *Vision Res.* 36, 3383–3395.
- Cohen, A.I. (1961). The fine structure of the extrafoveal receptors of the Rhesus monkey. *Exp. Eye Res.* 1, 128–136.
- Coppola, D., and Purves, D. (1996). The extraordinarily rapid disappearance of entoptic images. *Proc. Natl. Acad. Sci. USA* 93, 8001–8004.
- Curcio, C.A., Sloan, K.R., Kalina, R.E., and Hendrickson, A.E. (1990). Human photoreceptor topography. *J. Comp. Neurol.* 292, 497–523.
- de Ruyter van Steveninck, R.R., and Laughlin, S.B. (1996). The rate of information transfer at graded-potential synapses. *Nature* 379, 642–645.
- Do, M.T.H., Kang, S.H., Xue, T., Zhong, H., Liao, H.W., Bergles, D.E., and Yau, K.-W. (2009). Photon capture and signalling by melanopsin retinal ganglion cells. *Nature* 457, 281–287.
- Dowling, J.E. (1965). Foveal receptors of the monkey retina: fine structure. *Science* 147, 57–59.
- Drasdo, N., Millican, C.L., Katholi, C.R., and Curcio, C.A. (2007). The length of Henle fibers in the human retina and a model of ganglion receptive field density in the visual field. *Vision Res.* 47, 2901–2911.
- Edgington, D.R., and Stuart, A.E. (1979). Calcium channels in the high resistivity axonal membrane of photoreceptors of the giant barnacle. *J. Physiol.* 294, 433–445.
- Emanuel, A.J., and Do, M.T.H. (2015). Melanopsin tristability for sustained and broadband phototransduction. *Neuron* 85, 1043–1055.
- Eyal, G., Verhoog, M.B., Testa-Silva, G., Deitcher, Y., Lodder, J.C., Benavides-Piccione, R., Morales, J., DeFelipe, J., de Kock, C.P., Mansvelder, H.D., and Segev, I. (2016). Unique membrane properties and enhanced signal processing in human neocortical neurons. *eLife* 5, e16553.
- Finlay, B.L., Silveira, L.C.L., and Reichenbach, A. (2005). Comparative aspects of visual system development. In *The Primate Visual System: A Comparative Approach*, J. Kremers, ed. (John Wiley & Sons).
- Franco, E.C., Finlay, B.L., Silveira, L.C., Yamada, E.S., and Crowley, J.C. (2000). Conservation of absolute foveal area in New World monkeys. A constraint on eye size and conformation. *Brain Behav. Evol.* 56, 276–286.
- Gayet-Primo, J., Yaeger, D.B., Khanjian, R.A., and Puthussery, T. (2018). Heteromeric Kv2/Kv8.2 channels mediate delayed rectifier potassium currents in primate photoreceptors. *J. Neurosci.* 38, 3414–3427.
- Giarmarco, M.M., Cleghorn, W.M., Sloat, S.R., Hurley, J.B., and Brockerhoff, S.E. (2017). Mitochondria maintain distinct Ca²⁺ pools in cone photoreceptors. *J. Neurosci.* 37, 2061–2072.
- Gidon, A., Zolnik, T.A., Fidzinski, P., Bolduan, F., Papoutsi, A., Poirazi, P., Holtkamp, M., Vida, I., and Larkum, M.E. (2020). Dendritic action potentials and computation in human layer 2/3 cortical neurons. *Science* 367, 83–87.
- Govardovskii, V.I., Fyhrquist, N., Reuter, T., Kuzmin, D.G., and Donner, K. (2000). In search of the visual pigment template. *Vis. Neurosci.* 17, 509–528.
- Han, Y., Jacoby, R.A., and Wu, S.M. (2000). Morphological and electrophysiological properties of dissociated primate retinal cells. *Brain Res.* 875, 175–186.
- Harmening, W.M. (2017). [Contrast sensitivity and visual acuity in animals]. *Ophthalmologe* 114, 986–996.
- Harmening, W.M., Nikolay, P., Orlowski, J., and Wagner, H. (2009). Spatial contrast sensitivity and grating acuity of barn owls. *J. Vis.* 9, 13.
- Hass, C.A., Angueyra, J.M., Lindblom-Brown, Z., Rieke, F., and Horwitz, G.D. (2015). Chromatic detection from cone photoreceptors to V1 neurons to behavior in rhesus monkeys. *J. Vis.* 15, 1.
- Herculano-Houzel, S., Collins, C.E., Wong, P., and Kaas, J.H. (2007). Cellular scaling rules for primate brains. *Proc. Natl. Acad. Sci. USA* 104, 3562–3567.
- Hoang, Q.V., Linsenmeier, R.A., Chung, C.K., and Curcio, C.A. (2002). Photoreceptor inner segments in monkey and human retina: mitochondrial density, optics, and regional variation. *Vis. Neurosci.* 19, 395–407.
- Hoffman, D.P., Shtengel, G., Xu, C.S., Campbell, K.R., Freeman, M., Wang, L., Milkie, D.E., Pasolli, H.A., Iyer, N., Bogovic, J.A., et al. (2020). Correlative three-

- dimensional super-resolution and block-face electron microscopy of whole vitreously frozen cells. *Science* 367, eaaz5357.
- Holzman, D., and Yuste, R. (2015). The new nanophysiology: regulation of ionic flow in neuronal subcompartments. *Nat. Rev. Neurosci.* 16, 685–692.
- Hsu, A., Tsukamoto, Y., Smith, R.G., and Sterling, P. (1998). Functional architecture of primate cone and rod axons. *Vision Res.* 38, 2539–2549.
- Hudspeth, A.J., Poo, M.M., and Stuart, A.E. (1977). Passive signal propagation and membrane properties in median photoreceptors of the giant barnacle. *J. Physiol.* 272, 25–43.
- Jusuf, P.R., Lee, S.C., Hannibal, J., and Grünert, U. (2007). Characterization and synaptic connectivity of melanopsin-containing ganglion cells in the primate retina. *Eur. J. Neurosci.* 26, 2906–2921.
- Kay, A.R. (1992). An intracellular medium formulary. *J. Neurosci. Methods* 44, 91–100.
- Kim, K.J., and Rieke, F. (2001). Temporal contrast adaptation in the input and output signals of salamander retinal ganglion cells. *J. Neurosci.* 21, 287–299.
- Koch, C. (1999). *Biophysics of Computation: Information Processing in Single Neurons* (Oxford University).
- Kuang, X., Poletti, M., Victor, J.D., and Rucci, M. (2012). Temporal encoding of spatial information during active visual fixation. *Curr. Biol.* 22, 510–514.
- Lasater, E.M., Normann, R.A., and Kolb, H. (1989). Signal integration at the pedicle of turtle cone photoreceptors: an anatomical and electrophysiological study. *Vis. Neurosci.* 2, 553–564.
- Lee, S.C., and Grünert, U. (2007). Connections of diffuse bipolar cells in primate retina are biased against S-cones. *J. Comp. Neurol.* 502, 126–140.
- Lockhart, M.E. (1976). Morphological studies of deep and shallow avian foveas: a quantitative analysis. Doctoral dissertation (University of Massachusetts Amherst).
- Major, G., Larkman, A.U., Jonas, P., Sakmann, B., and Jack, J.J. (1994). Detailed passive cable models of whole-cell recorded CA3 pyramidal neurons in rat hippocampal slices. *J. Neurosci.* 14, 4613–4638.
- Masland, R.H. (2017). Vision: two speeds in the retina. *Curr. Biol.* 27, R303–R305.
- McMahon, M.J., Lankheet, M.J., Lennie, P., and Williams, D.R. (2000). Fine structure of parvocellular receptive fields in the primate fovea revealed by laser interferometry. *J. Neurosci.* 20, 2043–2053.
- Mennerick, S., Zenisek, D., and Matthews, G. (1997). Static and dynamic membrane properties of large-terminal bipolar cells from goldfish retina: experimental test of a compartment model. *J. Neurophysiol.* 78, 51–62.
- Mitkus, M., Olsson, P., Toomey, M.B., Corbo, J.C., and Kelber, A. (2017). Specialized photoreceptor composition in the raptor fovea. *J. Comp. Neurol.* 525, 2152–2163.
- Mitkus, M., Potier, S., Martin, G.R., Duriez, O., and Kelber, A. (2018). Raptor vision. *Oxford Research Encyclopedia of Neuroscience* (Oxford University), p. 40.
- Neher, E. (1992). Correction for liquid junction potentials in patch clamp experiments. *Methods Enzymol.* 207, 123–131.
- Niven, J.E., and Laughlin, S.B. (2008). Energy limitation as a selective pressure on the evolution of sensory systems. *J. Exp. Biol.* 211, 1792–1804.
- O'Brien, J.J., Chen, X., Macleish, P.R., O'Brien, J., and Massey, S.C. (2012). Photoreceptor coupling mediated by connexin36 in the primate retina. *J. Neurosci.* 32, 4675–4687.
- Okawa, H., Sampath, A.P., Laughlin, S.B., and Fain, G.L. (2008). ATP consumption by mammalian rod photoreceptors in darkness and in light. *Curr. Biol.* 18, 1917–1921.
- Pallotto, M., Watkins, P.V., Fubara, B., Singer, J.H., and Briggman, K.L. (2015). Extracellular space preservation aids the connectomic analysis of neural circuits. *eLife* 4, e08206.
- Peng, Y.R., Shekhar, K., Yan, W., Herrmann, D., Sappington, A., Bryman, G.S., van Zyl, T., Do, M.T.H., Regev, A., and Sanes, J.R. (2019). Molecular classification and comparative taxonomies of foveal and peripheral cells in primate retina. *Cell* 176, 1222–1237.e22.
- Perry, V.H. (1990). The distribution of cones in the primate retina. *Advances in Photoreception: Proceedings of a Symposium on Frontiers of Visual Science* (National Academies), pp. 114–116.
- Perry, V.H., and Cowey, A. (1988). The lengths of the fibres of Henle in the retina of macaque monkeys: implications for vision. *Neuroscience* 25, 225–236.
- Pitkow, X., Sompolinsky, H., and Meister, M. (2007). A neural computation for visual acuity in the presence of eye movements. *PLoS Biol.* 5, e331.
- Polyak, S.L. (1941). *The Retina* (The University of Chicago).
- Pong, M., and Fuchs, A.F. (2000). Characteristics of the pupillary light reflex in the macaque monkey: metrics. *J. Neurophysiol.* 84, 953–963.
- Rall, W., Burke, R.E., Holmes, W.R., Jack, J.J., Redman, S.J., and Segev, I. (1992). Matching dendritic neuron models to experimental data. *Physiol. Rev.* 72 (4, Suppl), S159–S186.
- Rao, R., Buchsbaum, G., and Sterling, P. (1994). Rate of quantal transmitter release at the mammalian rod synapse. *Biophys. J.* 67, 57–63.
- Reymond, L. (1985). Spatial visual acuity of the eagle *Aquila audax*: a behavioural, optical and anatomical investigation. *Vision Res.* 25, 1477–1491.
- Rodieck, R.W. (1998). *The First Steps in Seeing* (Sinauer Associates).
- Roth, A., and Häusser, M. (2001). Compartmental models of rat cerebellar Purkinje cells based on simultaneous somatic and dendritic patch-clamp recordings. *J. Physiol.* 535, 445–472.
- Rovamo, J., Raninen, A., and Donner, K. (1999). The effects of temporal noise and retinal illuminance on foveal flicker sensitivity. *Vision Res.* 39, 533–550.
- Rucci, M. (2008). Fixational eye movements, natural image statistics, and fine spatial vision. *Network* 19, 253–285.
- Sajdak, B.S., Salmon, A.E., Litts, K.M., Wells, C., Allen, K.P., Dubra, A., Merriman, D.K., and Carroll, J. (2019). Evaluating seasonal changes of cone photoreceptor structure in the 13-lined ground squirrel. *Vision Res.* 158, 90–99.
- Samorajski, T., Ordy, J.M., and Keefe, J.R. (1966). Structural organization of the retina in the tree shrew (*Tupaia glis*). *J. Cell Biol.* 28, 489–504.
- Savchenko, L.P., Poo, M.M., and Rusakov, D.A. (2017). Electrodiffusion phenomena in neuroscience: a neglected companion. *Nat. Rev. Neurosci.* 18, 598–612.
- Schein, S.J. (1988). Anatomy of macaque fovea and spatial densities of neurons in foveal representation. *J. Comp. Neurol.* 269, 479–505.
- Schnapf, J.L., Nunn, B.J., Meister, M., and Baylor, D.A. (1990). Visual transduction in cones of the monkey *Macaca fascicularis*. *J. Physiol.* 427, 681–713.
- Schneeweis, D.M., and Schnapf, J.L. (1999). The photovoltage of macaque cone photoreceptors: adaptation, noise, and kinetics. *J. Neurosci.* 19, 1203–1216.
- Sharpe, L.T., Stockman, A., Jagla, W., and Jägle, H. (2005). A luminous efficiency function, $V^*(\lambda)$, for daylight adaptation. *J. Vis.* 5, 948–968.
- Shen, G.Y., Chen, W.R., Midtgård, J., Shepherd, G.M., and Hines, M.L. (1999). Computational analysis of action potential initiation in mitral cell soma and dendrites based on dual patch recordings. *J. Neurophysiol.* 82, 3006–3020.
- Sinha, R., Hoon, M., Baudin, J., Okawa, H., Wong, R.O.L., and Rieke, F. (2017). Cellular and circuit mechanisms shaping the perceptual properties of the primate fovea. *Cell* 168, 413–426.e12.
- Stalmans, P., Delaey, C., de Smet, M.D., van Dijkman, E., and Pakola, S. (2010). Intravitreal injection of microplasmin for treatment of vitreomacular adhesion: results of a prospective, randomized, sham-controlled phase II trial (the MIVI-IIT trial). *Retina* 30, 1122–1127.
- Van Essen, D.C., Newsome, W.T., and Maunsell, J.H. (1984). The visual field representation in striate cortex of the macaque monkey: asymmetries, anisotropies, and individual variability. *Vision Res.* 24, 429–448.
- van Hateren, J.H., and van der Schaaf, A. (1998). Independent component filters of natural images compared with simple cells in primary visual cortex. *Proc. Biol. Sci.* 265, 359–366.

- Van Hook, M.J., Navy, S., and Thoreson, W.B. (2019). Voltage- and calcium-gated ion channels of neurons in the vertebrate retina. *Prog. Retin. Eye Res.* 72, 100760.
- van Welie, I., Wadman, W.J., and van Hooft, J.A. (2005). Low affinity block of native and cloned hyperpolarization-activated I_h channels by Ba^{2+} ions. *Eur. J. Pharmacol.* 507, 15–20.
- Veilleux, C.C., and Kirk, E.C. (2014). Visual acuity in mammals: effects of eye size and ecology. *Brain Behav. Evol.* 83, 43–53.
- Volland, S., and Williams, D.S. (2018). Preservation of photoreceptor nanostructure for electron tomography using transcardiac perfusion followed by high-pressure freezing and freeze-substitution. *Adv. Exp. Med. Biol.* 1074, 603–607.
- Vugler, A.A. (2010). Progress toward the maintenance and repair of degenerating retinal circuitry. *Retina* 30, 983–1001.
- Walls, G.L. (1942). *The Vertebrate Eye and Its Adaptive Radiations* (Hafner Publishing Company).
- White, J.A., Rubinstein, J.T., and Kay, A.R. (2000). Channel noise in neurons. *Trends Neurosci.* 23, 131–137.
- Williams, D.R., Artal, P., Navarro, R., McMahon, M.J., and Brainard, D.H. (1996). Off-axis optical quality and retinal sampling in the human eye. *Vision Res.* 36, 1103–1114.
- Yagi, T., and Macleish, P.R. (1994). Ionic conductances of monkey solitary cone inner segments. *J. Neurophysiol.* 71, 656–665.
- Yu, D.Y., Cringle, S.J., and Su, E.N. (2005). Intraretinal oxygen distribution in the monkey retina and the response to systemic hyperoxia. *Invest. Ophthalmol. Vis. Sci.* 46, 4728–4733.

STAR★METHODS

KEY RESOURCES TABLE

REAGENT or RESOURCE	SOURCE	IDENTIFIER
Antibodies		
Mouse anti-CtBP2 (shared epitope with ribeye)	BD Biosciences	612044; RRID: AB_399431
Alexa 555-conjugated goat anti-mouse	Thermo Fisher	A21127; AB_2535769
Biological Samples		
Macaque retinas (<i>Macaca mulatta</i> , 3–14 years of age; <i>Macaca fascicularis</i> , 3–9 years of age)	This paper	N/A
Chemicals, Peptides, and Recombinant Proteins		
Penicillin-streptomycin	Millipore-Sigma	P4333
Ames medium	Millipore-Sigma	A1420
Tetrodotoxin	Alomone Labs	T550
4-aminopyridine	Millipore-Sigma	A78403 or A275875
Kynurenic acid	Millipore-Sigma	K3375
Picrotoxin	Millipore-Sigma or R&D Systems	P1675 or 1128, respectively
Strychnine	Millipore-Sigma	S0532
D,L-2-Amino-4-phosphonobutyric acid	Tocris or Millipore- Sigma	0101 or A1910, respectively
Alexa fluor 488 hydrazide	Thermo Fisher	A10436
Alexa fluor 555 hydrazide	Thermo Fisher	A20501MP
Neurobiotin	Vector Labs	SP1120
Human plasmin	Millipore-Sigma	P1867
Papain	Worthington	LS003119
Trypsin inhibitor (ovomucoid)	Worthington	LS003087
Bovine serum albumin	Millipore-Sigma	A8806
DNase I (Deoxyribonuclease I)	Millipore-Sigma or Worthington	DN25 or LS006333, respectively
Software and Algorithms		
Igor Pro	WaveMetrics	https://www.wavemetrics.com
DataAccess	Bruxton	https://www.bruxton.com/
NEURON	https://neuron.yale.edu	https://neuron.yale.edu/neuron/
R	R Foundation for Statistical Computing	http://www.R-project.org/
Other		
Borosilicate capillary glass	A-M Systems	603500

RESOURCE AVAILABILITY

Lead Contact

Requests for further information, resources, and reagents should be directed to the Lead Contact, Michael Do (michael.do@childrens.harvard.edu).

Materials Availability

This study did not generate new unique reagents.

Data and Code Availability

Raw data and analysis routines are available upon request to the Lead Contact, Michael Do (michael.do@childrens.harvard.edu).

EXPERIMENTAL MODEL AND SUBJECT DETAILS

All procedures were approved by the Animal Care and Use Committees of institutions that provided tissue and Boston Children's Hospital. Macaques (*Macaca mulatta*, 3-14 years of age; *Macaca fascicularis*, 3-9 years of age) of both sexes were used. Animals were euthanized for purposes unrelated to the present study. Most had prior experimental histories but none had known vision problems. No findings reported here were observed to covary with animal age, sex, or experimental history.

METHOD DETAILS

Tissue collection

Eyes were removed pre-mortem under deep anesthesia whenever possible or post-mortem (usually < 15 min but never > 60 min). The eye was hemisected in the coronal plane, vitreous humor removed mechanically, and the posterior eyecup submerged in oxygenated media (see below). These procedures were completed within 5 minutes of eye removal. Eyecups were transported to the laboratory in darkness (requiring 15-90 min). The findings reported here appear to be independent of tissue ischemic time and time elapsed since eye removal.

Solutions

External solutions had osmolarities of 280-285 mOsm unless otherwise noted. Bicarbonate-buffered solutions were supplemented with penicillin (80-96 U·ml⁻¹) as well as streptomycin (0.080-0.096 mg·ml⁻¹; Millipore-Sigma P4333) and equilibrated with carbogen (95% O₂ and 5% CO₂) for a pH of 7.4 at 35°C. The standard external solution was bicarbonate-buffered Ames medium (Millipore-Sigma). For tissue transport and culture, the glucose concentration of Ames was sometimes increased from 6 to 24 mM. For microdissection, tissue perfusion sometimes used a simplified, "ionic Ames" medium (Do et al., 2009) (in mM: 120 NaCl, 3.1 KCl, 0.5 KH₂PO₄, 1.2 CaCl₂, 1.2 MgSO₄, 6 glucose, and 22.6 NaHCO₃). "HEPES Ames" was ionic Ames buffered with 10 mM HEPES rather than bicarbonate (with NaCl increased to 140 mM; pH 7.4 with NaOH). Trituration solution (Do et al., 2009) contained (in mM) 70 Na₂SO₄, 2 K₂SO₄, 10 glucose, 85 sucrose, 5 MgCl₂, and 10 HEPES (pH 7.4 with NaOH; 305 mOsm).

The solution for blocking all voltage-gated ion channels was a modified ionic Ames (in mM): 23.8 NaCl, 3.6 KCl, 1.2 MgCl₂, 6 glucose, 22.6 NaHCO₃, 0.0001 tetrodotoxin, 10 CsCl, 2 CoCl₂, 80 tetraethylammonium (TEA)-Cl, and 10 4-aminopyridine. Sulfate and phosphate were omitted to improve cobalt solubility. NaCl was reduced to maintain osmolarity.

For isolating I_{Kx}, the control solution contained (in mM): 107 NaCl, 10 N-Methyl-D-Glucamine-Cl, 3 CsCl (to block I_h), 3.6 KCl, 1.2 CoCl₂ (substituted for CaCl₂ to suppress Ca²⁺ and Ca²⁺-activated currents), 1.2 MgCl₂, 6 glucose, and 22.6 NaHCO₃. I_{Kx} was blocked by replacement of N-Methyl-D-Glucamine-Cl with TEA-Cl.

For isolating I_h, the control solution contained (in mM): 117 NaCl, 3 N-Methyl-D-Glucamine-Cl, 3.6 KCl, 1.2 CaCl₂, 1.2 MgCl₂, 6 glucose, 22.6 NaHCO₃, and 0.3 BaCl₂; pH 7.2 with HCl. I_h was blocked by the replacement of N-Methyl-D-Glucamine-Cl with CsCl. Ba²⁺ was included to block inward rectifier K⁺ channels, whose block by extracellular Cs⁺ can interfere with the isolation of I_h. 0.3 mM Ba²⁺ mildly blocks I_h itself (~10%) (van Welie et al., 2005).

To minimize the chance that observed effects were due to circuit interactions, solutions for experiments on I_{Kx} and I_h also included synaptic antagonists (in mM: 3 kynurenic acid, 0.1 picrotoxin, 0.01 strychnine, and 0.1 D,L-2-Amino-4-phosphonobutyric acid) (Emanuel and Do, 2015).

The pipette (electrode) solution contained (in mM) 97 K-methanesulfonate, 13 NaCl, 2 MgCl₂, 1 CaCl₂, 10 EGTA, 10 HEPES, 0.3 Na-GTP, 4 Mg-ATP, 7 phosphocreatine di(tris), and 2 L-glutathione (pH 7.2 with KOH, bringing [K⁺] to 118 mM; 275 mOsm). Conductivity was 1.4 µS·µm⁻¹ at 25°C (equivalent to 14 mS·cm⁻¹ and 71.4 ± 0.4 Ω·cm; measured with an Orion Star A215 and DuraProbe 4-cell sensor). Cones recorded in the retina were labeled for visualization while live (400 µM Alexa 488 hydrazide or 50 µM Alexa 555 hydrazide) and/or after fixation (0.5%-1.5% Neurobiotin; Vector Labs).

Tissue culture and microdissection

All procedures on live tissue were carried out under infrared illumination. If vitreous humor remained after the gross dissection, its removal was sometimes facilitated by application of human plasmin (Stalmans et al., 2010) (Sigma P1867; 1-2 µM in Ames medium, 23 or 35°C, 20-30 min). Eyecups were dark-adapted for > 1 hr at 33°C before experimentation began and were kept for ≤ 48 hr total. Tissue was removed from the eyecup as needed.

Cones were dissociated from the retina using procedures that were informed by prior reports (Han et al., 2000; Yagi and Macleish, 1994). The fovea (centered in a ~5-mm² piece of retina) or peripheral retina (≥ 8 mm from the fovea, also taken in a ~5-mm² piece) was dissected from the sclera and, in some cases, retinal pigment epithelium (RPE). Tissue was incubated for 15 min in papain (Worthington, 20-31 U·ml⁻¹; L-cysteine was usually omitted but sometimes included at 3 mM; 35°C) and then washed with Ames medium (often containing 1 mg·ml⁻¹ ovomucoid trypsin inhibitor and 1 mg·ml⁻¹ bovine serum albumin; 23°C; Worthington and Millipore-Sigma, respectively). In some instances, DNase I was included in the incubation or washes to reduce cell clumping (Millipore-Sigma DN25 at 120-200 U·ml⁻¹ or Worthington LS006333 at 120 U·ml⁻¹). Tissue was transferred into trituration solution and dispersed by passage through fire-polished glass pipettes of sequentially smaller bore. An aliquot of the cell suspension was placed in the recording chamber and mixed with HEPES Ames. Following cell adhesion, media was continually superfused (~2 ml·min⁻¹).

For recordings in tissue, the retina was removed from RPE and mounted with cones facing upward on a coverslip coated with poly-L-lysine, and then continually superfused ($5\text{--}8 \text{ ml}\cdot\text{min}^{-1}$). A platinum-iridium harp strung with Lycra fibers sometimes provided additional stabilization. In a few cases, $120\text{--}200 \text{ U}\cdot\text{ml}^{-1}$ DNase I (Millipore-Sigma; 24°C , 3–4 min) was used to weaken extracellular matrix and improve access to cones (Angueyra and Rieke, 2013). Eccentricity is given as the distance from the center of the fovea. The center was identified by its peak cone density and the convergence of cone axons.

Electrophysiological recordings

Cells were visualized with a $60\times$ water-immersion objective (1.0 NA) with differential interference contrast optics and infrared transillumination (center wavelength of 850 or 940 nm). Recordings were made at room temperature (23°C) for increased stability. For experiments near body temperature ($35\pm 2^\circ\text{C}$), the solution was warmed by an inline heater and monitored by a bath thermistor.

Electrophysiological recordings employed a Multiclamp 700B amplifier with a 4-pole, low-pass Bessel filter (10 kHz or 30 kHz for voltage clamp and 10 kHz for current clamp). For clarity, additional low-pass filtering was applied to I_{Kx} and I_{h} (100 Hz) and photocurrent (50 Hz). The sampling rate exceeded the Nyquist minimum. Pipettes were borosilicate glass (A-M Systems) and wrapped with parafilm to reduce capacitance to 3–6 pF, which was nullified electronically. Seals (generally $\geq 10 \text{ G}\Omega$) were formed on the IS/soma and/or terminal. Whenever possible (~50% of cells recorded in the retina), seal stability was confirmed by pulling an outside-out patch after recording. Pipette resistances were 3–12 M Ω and matched between IS and terminal for paired recordings. Series resistance (R_s) was generally $< 50 \text{ M}\Omega$. To accurately measure capacitance transients, R_s was uncompensated. 50% compensation was used for measuring I_{Kx} and I_{h} . A 6.5-mV junction potential has been corrected (Neher, 1992). For experiments involving current injection, the voltage drop across R_s was corrected offline.

Recordings were terminated or excluded from analysis if changes in cellular morphology were apparent; if R_s was $\geq 50 \text{ M}\Omega$ or varied by $\geq 50\%$; if baseline current was $\leq -200 \text{ pA}$ (for dissociated cones at -67 mV) or decreased by 30%; or if the voltage drift (generally $< 3 \text{ mV}$) was $> 10 \text{ mV}$. For recordings of IS τ_{slow} in the retina, a more stringent criterion for R_s ($\leq 20 \text{ M}\Omega$) was used because passive compartmental modeling indicated that higher R_s could artificially increase IS τ_{slow} . The more permissive R_s criterion was necessary for other experiments due to their low throughput. No dependencies of data on R_s were apparent.

Electrical stimulation

Gaussian white noise stimuli (sampled at 10 kHz) were set to drive each cell from -35 mV to -80 mV , bracketing the physiological range of photoreceptor light responses (roughly -40 mV to -70 mV in the various species examined) (Barnes, 1994; Okawa et al., 2008). The currents used had mean offsets as large as -50 pA and standard deviations as large as 450 pA . Changes in offset and standard deviation had only a mild effect on filter shape (i.e., small changes limited to $< 20 \text{ Hz}$) and no detectable effects on filter linearity and propagation fidelity. Stimuli typically lasted 50 s. The first 10 s allowed any response transients to settle and were not analyzed. The next 30 s were used to compute the linear filter as the cross-correlation of the stimulus and the response, normalized by the power spectrum of the stimulus (Baccus and Meister, 2002; Kim and Rieke, 2001). The cross-correlation was computed in partially overlapping, 5 s windows and averaged. The last 10 s period was not used for filter construction. It was convolved with the filter to give a predicted response for comparison with the actual, measured response. The filters were examined in the frequency domain to quantify response magnitude and phase lag (relative to the stimulus) as a function of temporal frequency. For stimulation with sine waves, there was no offset and amplitudes were -5 to -15 pA . Square steps of current were also delivered without an offset and had magnitudes scaled to drive the voltage over a range similar to that produced by Gaussian white noise.

Estimating terminal charging from IS responses

IS τ_{slow} was measured with voltage-clamp steps ($\pm 2.5\text{--}10 \text{ mV}$) from a holding potential of -67 mV . We found that IS τ_{slow} closely matched terminal τ and tracked parameters of propagation in dissociated cones (Figures 4A and 4B). These relationships are expected to hold for cones recorded in the retina if two conditions are met. The first is achieving voltage clamp of the terminal. Passive compartmental models suggest that clamp is effective: IS τ_{slow} remains strongly correlated with terminal τ and propagation fidelity when simulated cones are made more challenging to clamp by lengthening them or by imposing a ≥ 10 -fold lower internal conductivity (even when these manipulations produce unnaturally long values of IS τ_{slow} and multiplicative reductions of propagation fidelity; not shown). Further evidence for effective clamp is the similarity of passive properties estimated from cones in the retina and following dissociation, even though the former are clamped with one electrode at the IS and the latter with one electrode at each end (Figures 5C–5E). Additional evidence for adequate clamp can be found in setting the IS to voltages of different polarities and magnitudes while examining the terminal voltage. The terminal voltage scales linearly, indicating that voltage-gated currents are suppressed throughout the cell (Figure S4). Thus, it appears that foveal cones in the retina are well-clamped, satisfying one condition for interpreting IS τ_{slow} .

The second condition for inferring terminal τ from IS τ_{slow} is that the terminal is the slowest region to charge. We argue that this is the case for dissociated cones because the two parameters are nearly equal. For cones in the retina, IS τ_{slow} might reflect a compartment that is slower to charge than the terminal. The OS is one candidate. However, we found that charging times were similar for cones in the retina that retained their OS (compare Figures 4G and S5B). Another candidate is the electrically-coupled array of terminals from neighboring cones. The similar charging times of cones recorded in the retina and after dissociation argues against this possibility, consistent with the prior observation of weak electrical coupling among foveal cones (Sinha et al., 2017). The evidence for

effective voltage clamp and the relative slowness of terminal charging, taken together, indicates that IS τ_{Slow} provides an effective proxy for terminal τ and propagation fidelity for primate cones.

Voltage-gated current analysis

I_{Kx} and I_h were isolated by subtraction of currents remaining in TEA and Cs from those in control solutions, respectively (see above). This pharmacological approach was chosen because it was readily reversed (Figures S7A–S7D) and therefore allowed multiple cells to be analyzed in each piece of tissue. This was especially important for the fovea, whose tiny size makes it impractical to subdivide.

According to convention (Gayet-Primo et al., 2018), I_{Kx} was measured from tail currents evoked by a step from a test voltage to the baseline voltage of -30 mV. Current was averaged within a 2-ms window immediately after the step. I_{Kx} was also examined with a protocol involving steps from -90 mV. Due to its relative simplicity, this protocol is presented in Figures 7C (left), S7A, and S7B. I_h was measured as the average current (in a 200-ms window) at the end of steps to test voltages, from a baseline voltage of -30 mV.

To determine the extent to which I_{Kx} and I_h account for the difference in membrane conductivity between foveal and peripheral cones, the sizes of these currents at -67 mV (the voltage used for recordings that were the basis of passive compartmental models) was interpolated from the current-voltage relation of each cell. The current at -67 mV was multiplied by a correction factor of 2.5 for I_{Kx} (accounting for $\sim 40\%$ efficacy of 10 mM TEA block) (Beech and Barnes, 1989) and 1.1 for I_h (accounting for $\sim 10\%$ block by 300 μM barium; see above). These currents were converted to conductance using a reversal potential of -93 mV for I_{Kx} (the Nernst potential for K^+ in our recording conditions) and -30 mV for I_h (Biel et al., 2009). The latter is likely realistic given that Cs-sensitive tail currents were small at this voltage (Figure 7E). Dividing conductance by membrane surface area (estimated as the integral of the capacitance transient divided by a specific membrane capacitance of 0.01 $\text{pF} \cdot \mu\text{m}^{-2}$) yielded an I_{Kx} or I_h conductivity (at -67 mV). Figure 7G shows average differences between foveal and peripheral cones.

Visual stimulation

The light source was a 75-W xenon arc lamp, filtered to deplete heat, control intensity, and select wavelength in 10-nm bands (half-maximal transmission; center wavelengths are given). Stimulus timing was controlled by an electromechanical shutter. The stimulus was delivered through the microscope objective, forming a 300 - μm -diameter spot centered on the IS. To measure sensitivity, 20-ms flashes were calibrated in intensity to produce responses of < 10 pA, which are expected to produce responses in or near the linear range (Cao et al., 2014). Linearity was confirmed whenever possible. Dividing the amplitude of the response by the flash intensity gave the conventional measure of “dim-flash” sensitivity (in $\text{pA} \cdot \text{photons}^{-1} \cdot \mu\text{m}^2$). Cells were typically stimulated with a wavelength matching their peak wavelength sensitivity (λ_{max}). If not, intensity is expressed as the equivalent at λ_{max} , calculated using the known spectral sensitivities of macaque cones (Baylor et al., 1987; Govardovskii et al., 2000). Saturated responses are those that no longer increase in peak amplitude with increasing flash intensity.

Staining and immunohistochemistry

For imaging of neurobiotin-filled cones, retinas were fixed for 30 min in 4% paraformaldehyde in phosphate-buffered saline (PBS) at room temperature, washed with PBS, permeabilized with additional washes that included 0.3% Triton X-100 in PBS, and incubated overnight at 4°C in 4 $\mu\text{g} \cdot \text{ml}^{-1}$ streptavidin (coupled to Cy3 or Cy5; Jackson ImmunoResearch). The retinas were washed with 0.3% Triton X-100 in PBS (sometimes containing 3 $\mu\text{g} \cdot \text{ml}^{-1}$ DAPI for nuclei visualization) and then PBS. Retinas were mounted on glass slides in anti-fade medium (Vectashield) with plastic shims (~ 200 - μm thickness) to reduce compression by the coverslip.

For ribeye immunostaining, dissociated cones were fixed, permeabilized, and washed as above but in suspension, being pelleted by gravity or gentle centrifugation between steps. The cells were then dried onto slides. Subsequent steps were conducted by applying small pools of solution to the adhered cells within a humidified chamber. Cells were incubated in blocking solution (5% goat serum with 0.3% Triton X-100 in PBS) for 1 hr at room temperature. They were then exposed to a mouse monoclonal antibody that recognizes ribeye (anti-CtBP2; 1:1000; BD Biosciences 612044), which is well-characterized in the primate retina (Jusuf et al., 2007; Lee and Grünert, 2007). Following overnight incubation (4°C), cells were washed in blocking solution and then exposed to a goat anti-mouse secondary antibody coupled to Alexa 555 (1:500 for 3 hr; Thermo-Fisher). Cells were washed with blocking solution followed by PBS, and then mounted in anti-fade medium.

Imaging cellular morphology

For dissociated cones, z stacks were acquired with a CCD camera immediately before electrophysiological recording, stepping the objective in 1 - μm increments. Cones recorded in the retina were imaged live or after fixation. Confocal z stacks (steps of 0.4 - 1 μm , optical sections of 0.8 - 1.5 μm ; Zeiss LSM 510 or 710) were acquired with a $40 \times$ water-immersion objective (1.0 NA, Zeiss) in live or fixed tissue. Imaging was generally performed through the ganglion cell layer to avoid light scatter by photoreceptor outer segments. Retinal position and Alexa fluorescence were used to track individual cones from electrophysiological recording to imaging. Comparing cones live and after fixation indicates that there is negligible distortion of morphology by the latter. Cone dimensions were consistent with expectations from prior examinations by electron and light microscopy (Curcio et al., 1990; Drasdo et al., 2007; Hsu et al., 1998; Perry and Cowey, 1988).

Analysis of morphology

Morphological reconstruction was done in Igor Pro (WaveMetrics) using custom routines. The center of a cell was manually traced through the z stack and the diameter measured at each point. The position of each electrode was also measured.

Ribbon staining in the presynaptic terminals of dissociated cones was analyzed in paired transillumination and epifluorescence images. The axon was manually traced in small ($\sim 1\text{-}\mu\text{m}$) intervals for $15\text{ }\mu\text{m}$ from its ending, taking the diameter at each one. The average diameter was computed for the most distal $5\text{ }\mu\text{m}$ (encompassing the axon ending) and for the preceding $10\text{ }\mu\text{m}$. Their difference yielded the “ Δ Diameter” parameter in [Figure S1C](#). In the epifluorescence images, the ratio of fluorescence in the axon ending relative to the preceding $10\text{ }\mu\text{m}$ was calculated after subtraction of a baseline taken from regions outside the cell.

Electrical circuit models

Passive compartmental circuit models were generated in NEURON 7 using its standard integration method (backward Euler integration) ([Carnevale and Hines, 2009](#)). Cell morphology was loaded as four-dimensional coordinates (X, Y, Z, and diameter). Cells possessed 4-5 sections (IS, soma, axon, terminal, and sometimes an OS). Each section was subdivided into segments whose number followed the conventional rule of 10 per approximated alternating current length constant (λ_{AC}). This is an approximation because the equation assumes the resistive term to be negligible ([Carnevale and Hines, 2009](#)):

$$\lambda_{AC} = \frac{1}{2} \sqrt{\frac{(\text{section diameter}) \cdot (\text{internal conductivity})}{\pi \cdot \text{frequency} \cdot (\text{specific membrane capacitance})}}$$

The frequency was set to a conservative value ($\geq 500\text{ Hz}$). Increasing the number of segments had no apparent effect on responses, indicating that this rule is sufficient. A typical peripheral cone was represented as ~ 9 segments. A long foveal cone (e.g., $400\text{-}\mu\text{m}$ axon) was represented as 38 segments. Time steps were generally $0.1\text{ }\mu\text{s}$. $10\text{ }\mu\text{s}$ was sufficient for simulations that did not involve voltage clamp. Decreasing the time step further had no apparent effect. Membrane conductance was passive and had a linear (i.e., ohmic) current-voltage relation. The extracellular space was non-resistive and non-capacitive.

Responses used for model fitting were evoked by voltage-clamp steps ($\pm 2.5\text{-}10\text{ mV}$) delivered from -67 mV (as for the measurement of IS τ_{Slow}), except in the case of transients caused by membrane-patch rupture (see below). Models of dissociated cones were constrained by being simultaneously fit to responses measured in two or more configurations: single-site voltage clamp before second site break-in; IS and terminal voltages clamped with the identical command; IS voltage clamped and terminal voltage measured; and terminal voltage clamped and IS voltage measured. Model parameters did not covary with the subset of configurations used. Removal of individual or sets of configurations did not substantially alter best-fit values, which indicates that fits to single-site IS recordings (used for cones recorded in the retina) are sufficiently constrained (discussed further below). Voltage-clamp responses were verified to be linear (as in [Figure S4](#)), indicating negligible modulation of voltage-gated conductances and validity of the ohmic membrane conductance. Voltage responses to current injection were also examined. They appeared nonlinear even for small currents, suggesting that block of voltage-gated conductances would be required to isolate passive properties, as for other cell types ([Major et al., 1994](#); [Mennerton et al., 1997](#); [Roth and Häusser, 2001](#)). Blocking these conductances was undesirable because they shape the passive properties of primate cones ([Figures 7C–7G](#)). Thus, these responses were not used for modeling.

To determine passive properties when the cytosol was minimally perturbed, models were also fit to the capacitance transient produced when the membrane patch is ruptured for establishment of whole-cell recording. Rupture causes the membrane voltage to change from the cell’s baseline to that being commanded by the amplifier. Defining this voltage change ($\Delta V_{\text{Rupture}}$) is necessary for model fitting. We estimated it from the peak of the capacitance transient ($\Delta I_{\text{Rupture}}$): $\Delta V_{\text{Rupture}} = \Delta I_{\text{Rupture}} \cdot R_s$. The value of R_s was obtained from a subsequent voltage step for which ΔV was commanded and thus known. The estimate of $\Delta V_{\text{Rupture}}$ assumes that R_s does not change substantially from the time of rupture to the time of the first commanded voltage step (15–300 ms), which appears true for the analyzed cones. Using the integral of the capacitance transient to estimate $\Delta V_{\text{Rupture}}$ gave similar results.

For fitting models to cellular responses, biophysical free parameters were initialized to previous assumptions ([Hsu et al., 1998](#)): a membrane conductivity of $0.2\text{ pS}\cdot\mu\text{m}^{-2}$, an internal conductivity of $0.5\text{ }\mu\text{S}\cdot\mu\text{m}^{-1}$, and a specific membrane capacitance of $0.01\text{ pF}\cdot\mu\text{m}^{-2}$. R_s (generally initialized to $25\text{ M}\Omega$) contributed one additional free parameter for single-site recordings and two for dual-site recordings from dissociated cones. There were no other free parameters. The biophysical parameters were constrained to the same value throughout the cell. We consider this a reasonable simplification because our experiments indicate that current in one compartment evokes a similar voltage response across compartments. Additionally, allowing an uneven distribution of membrane conductivity produced only a subtle improvement in model fits (note the already close fits for models with uniform membrane conductivity, illustrated in [Figure 5B](#)). For pipette capacitance, values measured for each recording site in the cell-attached configuration were used. To incorporate R_s and pipette capacitance, the voltage- and current-clamp circuits of the amplifier were modeled. These circuits included linear filters matched in type and cut-off frequency to those used for data collection. For voltage clamp, R_s was a resistance between the cell and the amplifier. For current clamp, pipette capacitance was a capacitor to ground, placed between the R_s and amplifier. Adding capacitance to the voltage-clamp circuit or complexity to the pipette geometry had negligible effect.

Model fitting followed least-squares optimization, with free parameters pre-scaled by their logarithms to increase efficiency ([Shen et al., 1999](#)). Fits do not appear to be local minima because randomization and refitting gave the same values. To estimate the degree

to which estimates of biophysical parameters were constrained, fit error was measured as each parameter was varied from its best-fit value (with other parameters held at their best-fit values) (Shen et al., 1999). Fit error increased steeply with deviation from the best-fit value, suggesting that a unique minimum exists for each parameter (not shown). The only exception was the internal conductivity of peripheral cones recorded in the retina (by a single pipette at the IS). These internal conductivities ranged from 0.11 to 0.42 $\mu\text{S} \cdot \mu\text{m}^{-1}$, far lower than obtained in dual-site recordings of dissociated peripheral cones (mean \pm SEM of $1.1 \pm 0.1 \mu\text{S} \cdot \mu\text{m}^{-1}$) or foveal cones in any configuration ($1.3 \pm 0.6 \mu\text{S} \cdot \mu\text{m}^{-1}$). A likely explanation is that the short path length of the stout peripheral cone renders internal conductivity difficult to estimate by single-site recording. Thus, only dual-site recordings were used to assess the internal conductivity of peripheral cones.

To quantify signal propagation through modeled cones, a brief current pulse was simulated at the region of the IS farthest from the axon. The impulse responses (synonymous with the linear filter) at the IS and terminal were analyzed like other linear filters.

The dimensions of the “reference” cone used to assess the effect of varied biophysical parameters and morphology were (length \times diameter in μm): IS, 30×3.5 ; soma, 5.5×5.5 ; axon, 400×1.6 ; terminal, 7×4.5 . These parameters are characteristic of the longest and most slender foveal cones, observed within a few hundred microns of the center of the fovea (Curcio et al., 1990; Drasdo et al., 2007; Hsu et al., 1998; Perry and Cowey, 1988). The OS was omitted because it has a limited effect on propagation (Figure S6).

Length constant

The length constant (λ) provided in the legend for Figure 5 was calculated from the standard equation (Koch, 1999):

$$\lambda = \frac{1}{2} \sqrt{\frac{(\text{diameter}) \cdot (\text{internal conductivity})}{(\text{membrane conductivity})}}$$

We note that this equation is not strictly valid for structures, like foveal cones, that have sealed ends and non-uniformities in diameter. The sum of these divergences makes the attenuation predicted by λ modestly less than that observed experimentally and in passive compartmental models that incorporate realistic anatomy (not shown). Thus, the morphological details of foveal cones are likely to affect propagation.

Natural image model

To examine the propagation of responses during natural viewing, an image containing a broad range of spatial frequencies and contrasts was chosen from a database of luminance-calibrated photographs of natural scenes (van Hateren and van der Schaaf, 1998; image “imk03372.lmc”). The image size on the retina (4 pixels arcmin^{-1}) was set such that high spatial frequencies were present despite filtering by the optics of the eye. The image was upsampled for smoothness (to 24 pixels $\cdot \text{arcmin}^{-1}$). Various sinusoidal gratings were also generated to test how responses to specific spatial frequencies are propagated.

The optics of the eye were implemented by filtering with the astigmatism-corrected foveal modulation transfer function (Williams et al., 1996). The cone acceptance angle was modeled as a Gaussian of 0.01° radius (0.6 arcmin, as expected for a foveal cone of $\sim 2\text{-}\mu\text{m}$ IS diameter) (Chen et al., 1993; McMahon et al., 2000). The integral of the Gaussian was set equal to the cone effective collecting area of $0.6 \mu\text{m}^2$ (Hass et al., 2015; Schnapf et al., 1990; Schneeweis and Schnapf, 1999). Motion was simulated as a random walk of this receptive field across the image. The diffusion constant, $100 \text{ arcmin} \cdot \text{s}^{-1}$, mimics ocular drift during target fixation (Aytekin et al., 2014; Kuang et al., 2012; Pitkow et al., 2007). The position of the receptive field was updated every 0.5 ms by random and independent draws from the probability distributions for vertical and horizontal movement over the image lattice (Pitkow et al., 2007). For each position, the number of photoactivations (P^*) was calculated as the average photon density at each pixel (in $\text{photons} \cdot \mu\text{m}^{-2}$, see below) weighted by the Gaussian. This number was allowed to be non-integer to better accommodate the relatively small time step between positions. For display purposes, the instantaneous photoactivation rate (P^*/s) was calculated by dividing the number of photoactivations by the length of the time step.

The photon density at each pixel was calculated for a simulated red cone. To obtain image radiance, luminance was divided by the red cone contribution to the photopic luminosity function ($\sim 43\%$ of $683.002 \text{ lm} \cdot \text{W}^{-1}$, based on Stockman and Sharpe fundamentals) (Sharpe et al., 2005). To calculate irradiance, radiance was multiplied by the solid angle subtended by a macaque pupil (Hass et al., 2015). The pupil diameter (3 mm) corresponded to the value for the bright lighting condition of this simulation, where visual acuity is nearly maximal (Cavonius and Robbins, 1973; Pong and Fuchs, 2000). Photon flux density ($\text{photons} \cdot \mu\text{m}^{-2} \cdot \text{s}^{-1}$) was estimated by dividing irradiance by photon energy, taking into consideration the spectral sensitivity of red cones. Mean photon flux density across the scaled image corresponded to $1.9 \cdot 10^5 \text{ photoactivations} \cdot \text{s}^{-1}$. Photon density ($\text{photons} \cdot \mu\text{m}^{-2}$) was calculated by multiplying photon flux density by the 0.5-ms time step.

Phototransduction current was calculated by convolution of the photoactivation time series with a single-photon response. In the initial model (of Figure 1), the single-photon response of a foveal cone was estimated using published data. The fit to a single-photon response of a dark-adapted peripheral cone (Angueyra and Rieke, 2013) was stretched in time by 2-fold to match the longer duration of the response in foveal cones (Sinha et al., 2017). This fit was then scaled to the response amplitude expected from adaptation at the light level of the simulation (Angueyra and Rieke, 2013; Cao et al., 2014). The final model (of Figure 2) used the single-photon response recorded from a foveal cone (determined from the cell’s dim-flash response, as in Figure S6B, via division by the number of photoactivations produced by the flash). The fit to the single-photon response was scaled in amplitude according to

the expectation for adaptation. The single-photon response of foveal cones may be briefer because adaptation also speeds phototransduction kinetics (~20% for each 10-fold change in irradiance in peripheral cones) (Angueyra and Rieke, 2013). Nevertheless, testing the model with a 10-fold briefer single-photon response revealed little effect on propagation fidelity. The terminal response was within 10% of the IS response in magnitude, similar to the results presented in Figures 2F and 2G, as well as phase.

IS and terminal voltage were calculated by convolution of the phototransduction current with IS and terminal current-to-voltage filters. For the initial model, these filters were generated from a passive compartmental model with realistic foveal cone morphology (same dimensions as the reference cone, described above) and biophysical parameters that are the best estimates available prior to this study. The membrane conductivity was $2.45 \text{ pS} \cdot \mu\text{m}^{-2}$, based on prior measurements of peripheral cone morphology (Curcio et al., 1990; O'Brien et al., 2012) and input resistance (Schneeweis and Schnapf, 1999). Internal conductivity was set to $0.030 \text{ S} \cdot \text{m}^{-1}$, the only measurement available for a photoreceptor (Lasater et al., 1989). For the final model, IS and terminal filters were those directly measured from dissociated cones (Figures 2D and 2E).

Propagation fidelity was assessed by analyzing these filters in the frequency domain. The magnitude spectra of terminal and IS voltages were obtained and their ratio taken. This ratio was weighted by the magnitude spectrum of the photocurrent. Averaging the weighted ratio across temporal frequencies provided a measure of propagation fidelity. The same procedure was used for the phase spectra of terminal and IS voltages, giving ratios near 1 (not shown).

Note that several variables might affect the magnitude of the simulated response, such as screening of light by macular pigment and the spectral composition of the image. However, the estimate of propagation fidelity is independent of these factors. Because the effects of propagation are linear (Figures 2C and 2D), the ratios of terminal and IS response magnitude and phase remain constant.

QUANTIFICATION AND STATISTICAL ANALYSIS

Data were analyzed in Igor Pro (WaveMetrics). Molecular Devices files were imported with Bruxton DataAccess. Some statistics were calculated in R (R Foundation for Statistical Computing). Normality was assessed with Kolmogorov-Smirnov tests and parametric or non-parametric statistical tests were used as appropriate. Pearson correlation coefficients (r) were calculated after normalizing data to a mean of 0 and standard deviation of 1; p values are the proportion of 10^6 data shuffles in which $|r_{\text{shuffle}}| \geq |r|$. Locally estimated scatterplot smoothing (LOESS) regression was performed in Igor Pro using a built-in routine (smoothing factor of 0.8), which also gives 95% confidence intervals. For statistics on variation in IS τ_{Slow} with eccentricity (Figure 4F legend), 95% confidence intervals were obtained from bootstrapping (10,000 random resamplings, with replacement, of the IS τ_{Slow} versus eccentricity data).